Research Article

Musawenkhosi Patson Mkhatshwa* and Melusi Khumalo

Overlapping grid SQLM for third-grade modified nanofluid flow deformed by porous stretchable/shrinkable Riga plate

https://doi.org/10.1515/nleng-2022-0276 received July 22, 2022; accepted January 2, 2023

Abstract: The improvement in thermal performance of fluid and the control of energy loss are equitably significant. Therefore, the purpose of this study is to analyze entropy generation, stagnation point flow, and thermal characteristics of non-Newtonian third-grade modified hybrid nanofluid generated by a stretchable/shrinkable Riga plate in a porous medium with varying flow viscosity. In this analysis, a modification of hybrid nanofluid is considered by using pure water as a base fluid and three various nanomaterials (aluminium oxide, copper, and nickel) as nanoparticles in the characterization of heat transfer. Furthermore, the contribution of heat source/ sink and viscous dissipation are accounted for in the model. The suited transformations are enforced to remodel the governing mathematical equations to produce ordinary differential equations that are conveniently tackled *via* spectral quasilinearization method (SQLM) along with the overlapping grid idea to yield numerical solutions. The preference of this approach over others has been justified through discussion of error bound theorems, residual and solution errors, computational time, and conditioning of matrices. The physical significance of disparate governing parameters on flow variables, velocity gradient, thermal rate, and entropy generation are scrutinized through graphs and tables. Crucial findings of the study include that temperature of the modified hybrid nanofluid enhances quickly (better thermal conductor) than temperature of single nanofluid, hybrid nanofluid, and conventional third-grade fluid for higher Biot number, variable viscosity, and heat source

* Corresponding author: Musawenkhosi Patson Mkhatshwa,
Department of Mathematical Sciences, University of South Africa,
Cnr Christian, de Wet Rd and Pioneer Avenue, Florida Park, 1709,
Roodepoort, South Africa, e-mail: patsonmkhatshwa@gmail.com
Melusi Khumalo: Department of Mathematical Sciences, University
of South Africa, Cnr Christian, de Wet Rd and Pioneer Avenue,
Florida Park, 1709, Roodepoort, South Africa,
e-mail: khumam@unisa.ac.za

parameters. Mass suction enhances fluid flow and physical quantities of interest, but suppresses the fluid temperature. An increase in variable fluid viscosity, modified Hartmann number, and third-grade parameters enhances the wall drag coefficient while lowering the rate of heat transfer, and the opposite is true for porous media. More entropy is generated in the system by high variable fluid viscosity, suction, viscous dissipation, modified Hartman number, and non-Newtonian parameters. Owing to high velocity and temperature associated with modified hybrid nanoparticles, modified hybrid technology is recommended in enhancing the physical attributes of the fluid with minimal cost effects. In engineering and industrial point of view, this study can contribute significantly in thermal improvement of the working fluid.

Keywords: overlapping domain decomposition, spectral quasilinearization method, third-grade fluid, modified nanofluid model, porous medium, fluid viscosity variation, Riga plate, entropy generation

1 Introduction

Flows with regard to non-Newtonian fluids have been a topic worth researching in the recent past years because of their prominence in various industrial and engineering processes. Shampoos, soaps, muds, apple sauce, polymeric liquids, sugar solution, condensed milk, tomato paste, paints, and blood at low shear rate are typical materials with non-Newtonian fluids attributes. Nevertheless, their behaviour cannot be inspected via a single constitutive correlation because of their varying rheological properties. As a result, diverse fluid models have been introduced to delineate precise nature of non-Newtonian materials. The correlation among shear rate and shear stress is nonlinear in such materials. Third-grade fluid is a subcategory of differential kind non-Newtonian fluid that discloses shear thickening and shear thinning features. Thermodynamically stable conditions for third-grade fluid were established by Fosdick and Rajagopal [1].

Nonetheless, non-Newtonian fluids still fail to meet the demand for excellent heat transfer performance as their thermal conductivity is poor. To overcome such drawback, the idea of suspending nanoparticles (NPs) of diameter below 100 nm into the non-Newtonian fluid is quite innovative and helpful in improving the thermal conductivity along with heat transfer competency. These NPs can be found in the form of metals such as copper (Cu), silver (Ag), nickel (Ni) and gold (Au), metal oxides such as alumina/aluminium oxide (Al₂O₃), copper oxide (CuO), titania/titanium dioxide (TiO₂) and silicon dioxide (SiO₂), metal carbides, metal nitrides, and carbon materials such as graphite, single-walled carbon nanotubes, multi-walled carbon nanotubes (MWCNTs), and diamond [2]. The resultant fluid formed after dispersion of these NPs into base fluids such as water (H2O), glycol, and engine oil is called nanofluid. Important applications of nanofluids arise in disciplines where heat transfer or cooling is needed such as nuclear reactor cooling, solar collectors, automotive, refrigerators, electronic cooling, and heat exchangers. Choi and Eastman [3] were the first researchers to instigate the notion of nanofluid by highlighting the merits of using NPs to boost heat transmission. Subsequently, factors affecting thermal conductivity of nanofluid, which include stability, size, shape, temperature of the fluid, concentration of the suspended NPs, and type of the regular fluid used have been studied [4-6]. Thus far, numerous scholars [7-11] have used either Buongiorno model [12] or Tiwari and Das model [13] to inspect flow and heat transfer features in third-grade nanofluid via different geometries.

Although it is feasible to enhance features of single nanofluids (SNFs) by fluctuating the volume concentration of the nanomaterial, this is, however, restricted by the trouble in balancing the net positive of viscosity diminish versus the net negative viscosity upsurge. To circumvent this limitation, hybrid nanofluids (HNFs) have been developed, and distinctive features of various types of NPs have been exploited. HNF is a novel class of heat transmission fluid that is capable of outperforming the base fluid and SNF with regard to heat transference performance. In HNF model, two kind of NPs are suspended into a regular fluid, whereas in the SNF model only one type of NP is dispersed into the base fluid. Suresh et al. [14,15] initiated the conception of HNF via experiment and numerical results, which confirmed that HNF is the best heat transfer enhancer than SNF and regular fluid. HNFs have been found to be applicable in several technological and manufacturing processes. When coming up with a reliable HNF, it is necessary to choose an appropriate combination of NPs. The principal aim in developing HNF is to improve the properties of a single NP

that is either a better thermal conductor or possesses enhanced rheological features. For that reason, it make sense to blend a NP that has improved thermal conductivity with a NP that possesses augmented rheological properties. One way of achieving this aim is blending metallic NPs with metal oxides NPs. This is because metals such as Cu are known to be better thermal conductor and metal oxides such as Al₂O₃ are chemically inert and stable. Even though, metals are better thermal conductor, but they are costly and not realistic in mass production. Thus, using NPs in the form of metal oxides with metallic NPs can be massively pragmatic to the economy. So, the resultant HNF will be a better thermal conductor with intensified heat transfer competencies than metal oxide SNF, chemically inert, stable, and cheaper compared to the metal SNF. Devi and Devi [16] extended the Tiwari and Das model to accommodate thermo-physical attributes of HNF. HNF model has been extensively used with non-Newtonian fluids such as second- and third-grade fluids [17-20]. Govindarajulu and Reddy [20] inspected magnetohydrodynamic (MHD) pulsatile radiative flow of Au-Al₂O₃/blood third-grade HNF through a porous channel considering the consequences of viscous dissipation and Ohmic heating. Their valuable results include that flow fields diminish with large non-Newtonian parameter and Hartman number, but thermal fields improve with high viscous dissipation. Improving viscous dissipation enhances the heat transmission rate, which, however, diminishes with high magnetic field and heat radiative fluxes.

The ability to use two NPs to improve the characteristics of SNF has open more opportunities to test positive outcomes of suspending three solid NPs into the normal fluid. Recently, a novel class of working fluid called modified nanofluid (MNF) has been discovered as a superior heat transfer enhancer than base fluid, SNF, and HNF. Other words for the MNFs are tri-HNF and ternary nanofluid. In MNF, three kinds of particles with various thermophysical features and chemical bonds are suspended onto the regular fluid. To improve efficiency in a metal-metal oxide/metal oxide-metal HNF, another metal or metal oxide with different thermal or rheological properties can be added to produce metal-metal oxide-metal/metal oxide-metal-metal MNF. For example, in the Cu-Al₂O₃/ Al₂O₃-Cu HNF mentioned earlier, cost-effective metal NPs like Ni NPs can be added to give Cu-Al₂O₃-Ni/ Al₂O₃-Cu-Ni MNF model. Ni NPs have received considerable attention owing to their advantageous chemical, physical, and magnetic properties. Also, Ni NPs are very reactive, environmental friendly, and simple to operate, and that make them useful in diverse organic reactions including minimization of ketones and aldehydes, chemo-selective oxidizing coupling of thiols, α -alkylation of methyl ketone, synthesis of stilbenes from alcohol through Witting-kind olefination, and hydrogenation of olefins. Ni NPs find applications in diverse technological disciplines including ink for nanotube printings, biomedicine, magnetic materials, electronics, catalytic systems, augmented pseudo-capacitance, battery production, magnetic biocatalysts, adsorption of yellow dyes, biomolecules immobilization through the magnetic force of Ni NPs, optical switches, and field-modulated gratings. When collated with other NPs, Ni NPs possess substantial capability as catalysts in reactions. fibre formation, propellants, sintering additive in coatings, and plastics. An extensive review of synthesis, stability, thermo-physical features, heat relocation solicitation, and environmental consequences of MNF was done by Adun et al. [21]. Arif et al. [22] explored MNF with water as a base fluid considering three diverse shaped NPs. They reported that MNF demonstrates an ability to be heat transfer rate enhancer than HNF and SNF. Also, this heat transmission rate can be enhanced by close to 33.67%, which is an indicator of assuring thermal performance in the rate of heat transfer. References [23-25] entail recent studies on non-Newtonian MNF flow and heat transfer through various geometrical configurations.

The consequences of time-dependent fluid viscosity give rise to fluctuation in the properties of the fluid [26]. For instance, fluid viscosity drops with fluctuation in temperature, but viscosity of gases augments with intensifying temperature. In oily liquids, temperature increment results to friction that impacts the viscosity of the fluid, which is variant in nature. Due to this incompetency, several scholars have inspected the phenomena of variable viscosity effect subject to diverse conditions. Recent studies on the impact of variable viscosity on HNF and MNF flow over different geometries include [27–30]. Nadeem and Abbas [29] scrutinized the impact of timedependent viscosity on MHD flow and heat transfer characteristics of Al₂O₃-Cu-Ni/H₂O MNF via an exponential stretchable surface in porous media. They perceived that viscosity of the fluid is the inverse function. The same MNF model was used by Abass et al. [30] to investigate flow and heat transference over a nonlinear stretching Riga plate with time-dependent viscosity. They found that velocity depreciates for large values of positive viscosity variant parameter and appreciates for large values of negative variable viscosity parameter.

It has been established that consideration of porous matrix yields thermal insulation and enhancement of heat transmission. The significance of porous media in

the boundary layer flow has captured attention of many researchers owing to its practical use in oil production, cooling approach of nuclear reactors, heat exchangers, electronic cooling systems, geothermal engineering, and underground disposition of nuclear waste. In medicine, porous media plays a crucial role in transmission process in human lungs and kidneys, gall bladder in the existence of stone and clogging in arteries, and slight blood vessels that cannot be resisted. Hou et al. [23] analyzed flow, heat, and mass transmission in pseudo-plastic liquid composed of tri-hybrid NPs over a stretchable porous surface. Sohail et al. [24] scrutinized flow and heat transfer of pseudo-plastic liquid with tri-hybrid NPs through stretching sheet in porous media. Their valuable findings include that Darcy number causes slowness in the movement of fluid particles. Ramesh et al. [31] studied heat transport augmentation in the flow of ternary nanofluids via stretching convergent/divergent channel in porous media. Alharbi et al. [32] inspected flow, heat, and mass transfer over a moving cylinder with Darcy tri-hybrid nanomaterials. Other recent investigations on flow and heat transfer in porous medium via different geometrical configurations are found in refs [33-38].

Boundary conditions are practically crucial for defining a problem and, concurrently of principal significance in computational fluid dynamics. This is due to the fact that the applicability of numerical methods and the consequent quality of computations can critically be decided on how those are numerically treated. Convective boundary condition signify the rate of heat transmission via the surface, which is proportional to the local variation in temperature with ambient conditions. This means that convective boundary condition augments the temperature and consequently the thermal conductivity of nanofluids. For that reason, it is essential to take into consideration convective boundary condition as more appropriate model collated to isothermal conditions. Solicitations of convective boundary conditions can be found in diverse manufacturing devices including heat exchangers, atomic plants, gas turbines, and thermal energy storage [39]. These procedures gain highest temperature when the flow is subject to convective boundary conditions. In the latest past years, inspection of boundary layer flow and heat transfer problems accompanied by convective boundary conditions has been a subject of interest to many scholars [19,40,41], since first initiated by Aziz [42].

Attributes of magnetic flux induction arises in diverse engineering, geophysical, astrophysical, and industrial processes. Fluids such as plasma, electrolytes, and metals of liquid state to name a few, directly rest upon the induction of magnetic flux and electric field in the flow model. Fluids being poor-electromagnetic conductors due to increment in inductions are the justification for these aforesaid enclosure of electric and magnetic fields. An alternative to make fluids better conductors is the use of innovative Riga plate. A Riga palate is an electromagnetic actuator consisting of alternative electrodes and magnets deposited on a level surface. This innovative idea was initiated by Gailitis and Lielausis [43]. Khashi'ie et al. [17,18] scrutinized flow of Al₂O₃-Cu/water/ ethylene/methanol second-grade HNF via a Riga plate. They reported that hybrid NPs and the parameter of electro-magnetohydrodynamic (EMHD) contributes towards thermal upsurge of non-Newtonian working fluid. Also, second-grade parameter stipulates a remarkably negative influence on thermal performance. Siddique et al. [19] explored stagnation point flow and heat transmission of second-grade HNF (Al₂O₃ + Cu/engine oil) via a stretchable/shrinkable Riga wedge considering the impact of fuzzy NPs, heat generation, and radiative heat flux. Their core findings include that HNF is a superior thermal conductor than the convectional second-grade liquid. The aspects of porous media and variable fluid viscosity were not accounted for in the studies conducted by Khashi'ie et al. [17,18] and Siddique et al. [19]. Other recent explorations on flow and heat transfer analysis using HNF model via Riga plate are found in refs [44-47]. Unlike in the HNF model, limited research work (see [30]) is available in literature regarding the MNF flow model past a Riga plate.

Another aspect that works as an effectual tool to augment the performance of heat transfer procedures is entropy generation along with its depreciation. The minimization of entropy generation is appreciable in diverse thermal engineering systems including air separators, reactors, fuel cells, chillers, thermal solar, chemical, and electro-chemical. The excellent energy of the system is maintained through the application of the second law of thermodynamics. Upreti et al. [48] inspected entropy production and heat transmission of unsteady squeezing MHD HNF (CNTs and MWCNTs) flow between two parallel plates. They disclosed that entropy generation accelerates with escalation in values of magnetic field parameter as the HNFs moved away from the surface. Very few scholars [49-51] have make use of the second law scrutiny to reduce entropy production in MNF models subject to different physical attributes.

In light of the afore-stated surveys, no study has been reported on entropy generation, stagnation point flow, and thermal characteristics in non-Newtonian third-grade fluid comprising ternary hybrid NPs induced by a Riga plate in porous media with temperature-dependent viscosity. The

current study attempts to close this research gap, and for that reason, it is believed to be original and entails new significant components that have not been reported by other scholars. Accordingly, the intention of this work is to outstretch the theoretical study of Khaishi'ie et al. [18] by investigating entropy production, flow, and heat transfer in third-grade MNF near stagnation point via a stretchable/ shrinkable Riga plate in porous medium. The choice of third-grade fluid model instead of the second-grade model that was considered by Khaishi'ie et al. [18] is justified by the fact that second-grade fluid model its incapable of describing the shear thickening and thinning phenomena for the steady flow via rigid boundary. However, the thirdgrade fluid model signifies an additional, although inconclusive, strive towards a more complete explanation of the behaviour of viscoelastic fluids. Other novel features of the current scrutiny include consideration of varying flow viscosity, thermal convective boundary conditions, and heat source/sink effects. Also, because of remarkably literature and already highlighted advantages of Cu and Al₂O₃ NPs, both NPs have been chosen to be blended with useful Ni NPs that is limited in the literature to give an appropriate MNF model. The transformed ordinary differential equations (ODEs) are conveniently tackled via the spectral quasilinearization method (SQLM) along with the overlapping grid idea to yield numerical solutions. The SQLM has been extensively used to solve boundary layer flow problems because of its superior accuracy and convergence, which are achievable with least number of iterations. Since the SQLM approach is characterized by full differentiation matrices that can lead to dense coefficient matrix, the accuracy and convergence can deteriorate massively when many grid points are required and when the computational region is large. Applying the SQLM in overlapping multi-domains could be one possible way of ensuring that good spectral accuracy and convergence is always maintained, irregardless of the number of grid points used and the domain size. This is because overlapping scheme contribute towards sparsity of the coefficient matrix, thus becoming very easy to compute its inverse. Also, the propagation of round-off errors that can bring about unstable results is most likely to be depreciated through the usage of less grid points at each sub-domain. In the current study, the preference of this approach over the single-domain version of SQLM has been justified through discussion of residual and solution errors, computational time, and conditioning of matrices. Graphs and tables are utilized in demonstrating behaviour of emerging parameters against entropy generation, velocity, temperature, wall shear stress, and thermal transmission rate. The following crucial

research questions are expected to be answered by the considered scrutiny:

- What is the impact of hybridization of aluminium oxide, copper, and nickel NPs on the thermo-physical attributes of the third-grade MNF model?
- What is the contribution of considering the MNF model along with heat source/sink, viscous dissipation and convective boundary conditions on thermal performance of the fluid?
- What is the significance of control parameters including porosity, EMHD, fluctuating fluid viscosity, and suction/ injection on the third-grade MNF flow?
- How can embedding flow parameters be controlled to ensure adherence to the second law of thermodynamics (reduction of entropy generation)?
- What is the effect of control parameters on wall shear stress and heat transmission rate?
- What are the merits of choosing the overlapping grid SQLM instead of the single-domain SQLM when solving the non-dimensional transport equations?

The outcomes of this work are novel and play a crucial role in controlling energy loss within thermal devices, and further contribute towards ascertainment of the modified hybrid NPs' performance in the non-Newtonian third-grade fluid. Through results of this work, efficiency and proficiency of thermal energy systems can be hugely enhanced in various industrial, engineering, and biomedical disciplines at a low cost and environmental friendly way. The assessment of entropy generation finds solicitation in power engineering and aeronautical propulsion to anticipate the smartness of the overall system.

Problem statement

We account for stagnation point flow of non-Newtonian third-grade MNF (Al₂O₃-Cu-Ni/H₂O) generated by a stretchable/shrinkable horizontal Riga (EMHD) plate in a porous medium with existence of convective boundary constraint and suction/injection on the surface. The geometry of the current flow model is depicted in Figure 1. The subsequent suppositions are taken into account when developing the MNF mathematical model:

- From the theoretical point of view, the Riga plate is fabricated using electrodes and permanent magnets having the same widths w_n .
- The surface velocity of the fluid is denoted by $u_w(x) = cx$, where *c* is the coefficient of the velocity of the deformed plate. The constant c can be positive (stretchable Riga

- surface that assist the flow), negative (shrinkable Riga surface that opposes the flow) or zero (static Riga surface). On the other hand, the velocity of the ambient fluid is signified by $u_e(x) = ax$, where the constant a is always positive.
- In this problem, x represents the distance parallel to the sheet, v is the distance normal to the sheet, T_w denotes surface temperature for the nanofluid which is assumed to be constant, and T_{∞} represents ambient fluid temperature.
- · In the current nanofluid model, the conventional base liquid (pure water) and modified nanomaterials (Al₂O₃, Cu, Ni) are presumed to be in thermal equilibrium and stable with no slip occurring between them. The Al₂O₃-Cu-Ni/H₂O MNF model was also used by Abbas et al. [29,30] in the Newtonian case. In the SNF, HNF, and MNF models, one, two, and three solid nanomaterials are sequentially dispersed in a base fluid, respectively.
- The viscosity is presumed to be temperature variant, and the energy equation is modelled subject to heat omission/consumption.
- To control energy loss within the thermal devices, we also account for entropy production.

Adopting the aforestated suppositions, the governing boundary layer equations are as follows [18,19,44,52]:

$$\frac{\partial u}{\partial x} + \frac{\partial v}{\partial y} = 0, (2.1)$$

$$u\frac{\partial u}{\partial x} + v\frac{\partial u}{\partial y}$$

$$= u_{e}\frac{du_{e}}{dx} + \frac{1}{\rho_{mnf}}\frac{\partial}{\partial y}\left(\mu_{mnf}(T)\frac{\partial u}{\partial y}\right) - \frac{\mu_{mnf}(T)}{\rho_{mnf}k^{*}}u$$

$$+ \frac{\pi j_{0}M}{8\rho_{mnf}}\exp\left(-\frac{\pi}{b_{1}}y\right)$$

$$+ \frac{\alpha_{1}}{\rho_{mnf}}\left(u\frac{\partial^{3}u}{\partial x\partial y^{2}} + v\frac{\partial^{3}u}{\partial y^{3}} + \frac{\partial u}{\partial x}\frac{\partial^{2}u}{\partial y^{2}} + 3\frac{\partial u}{\partial y}\frac{\partial^{2}u}{\partial y^{2}}\right)$$

$$+ \frac{2\alpha_{2}}{\rho_{mnf}}\frac{\partial u}{\partial y}\frac{\partial^{2}u}{\partial x\partial y} + \frac{6\alpha_{3}}{\rho_{mnf}}\left(\frac{\partial u}{\partial y}\right)^{2}\frac{\partial^{2}u}{\partial y^{2}},$$
(2.2)

$$u\frac{\partial T}{\partial x} + v\frac{\partial T}{\partial y}$$

$$= \frac{\kappa_{mnf}}{(\rho C_p)_{mnf}} \frac{\partial^2 T}{\partial y^2} + \frac{Q_0(T - T_\infty)}{(\rho C_p)_{mnf}} + \frac{\mu_{mnf}(T)}{(\rho C_p)_{mnf}} \left(\frac{\partial u}{\partial y}\right)^2 + \frac{\alpha_1}{(\rho C_p)_{mnf}} \left(u\frac{\partial^3 u}{\partial x \partial y^2} + v\frac{\partial u}{\partial y}\frac{\partial^2 u}{\partial y^2}\right)$$

$$+ \frac{2\alpha_3}{(\rho C_p)_{mnf}} \left(\frac{\partial u}{\partial y}\right)^4.$$
(2.3)

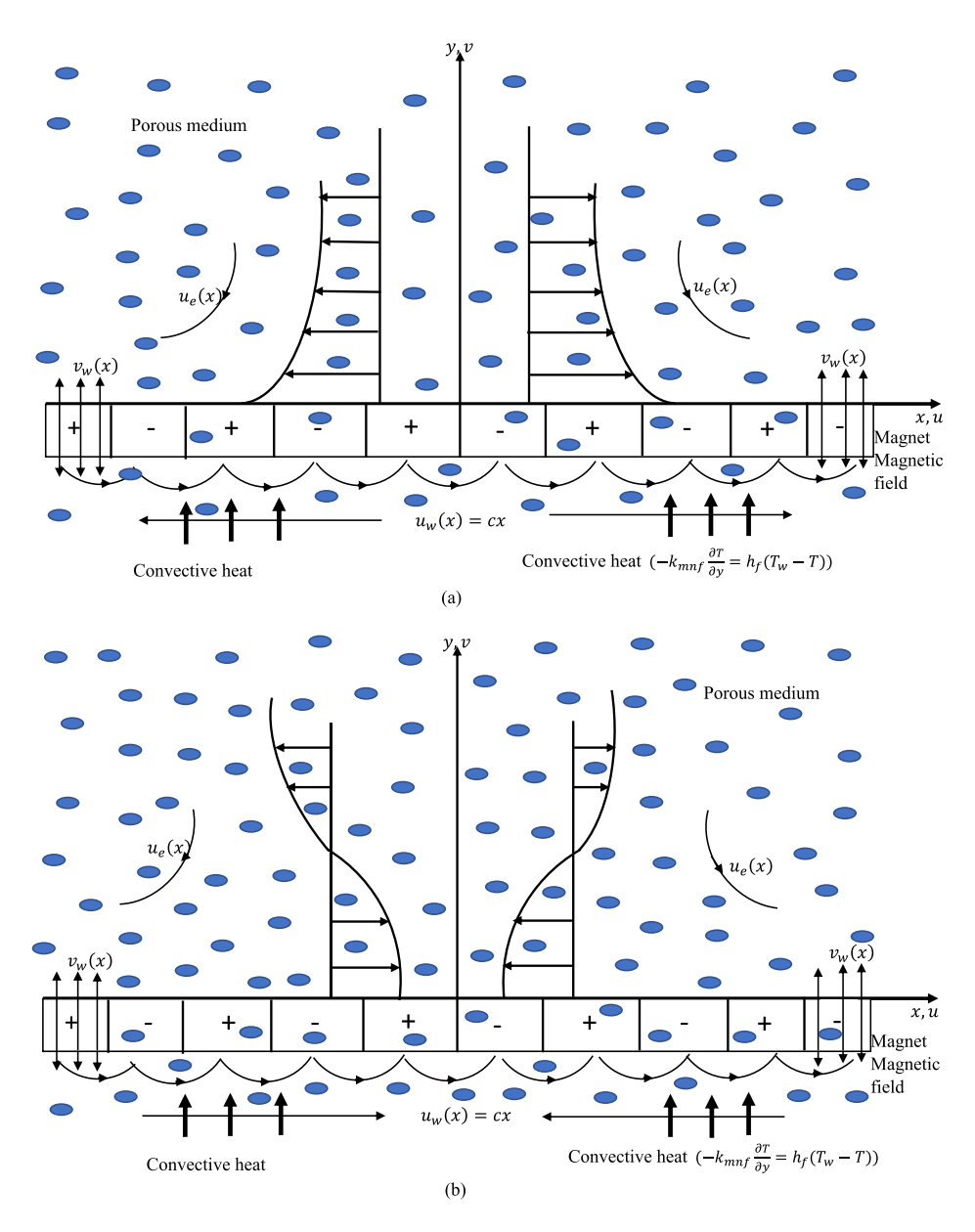


Figure 1: Geometry of the model. (a) Stretching surface, and (b) shrinking surface.

Here, u and v are the MNF velocity segments parallel to the x- and y-axes, respectively, α_1 , α_2 , and α_3 are the material parameters, k^* signifies permeability; j_0 , $M(=M_0x)$, and b_1 are applied current density in the electrodes, magnetization of the permanent magnets mounted on the Riga plate surface with M_0 being a constant for variable magnets magnetization, and width of electrodes and magnets, respectively; Q_0 is the heat source/sink coefficient; and ρ_{mnf} , μ_{mnf} , $(\rho C_p)_{mnf}$, and κ_{mnf} are the density, dynamic viscosity, specific heat at a constant pressure, and thermal conductivity of the MNF, respectively. The thermo-physical models of SNF, HNF, and MNF are depicted in Tables 1 and 2, whereas values of thermo-physical properties of nanomaterials along

with pure water are demonstrated in Table 3. The subscripts s1, s2, and s3 stand for solid NPs of Al_2O_3 , Cu, and Ni, respectively, whereas subscripts f, nf, hnf, and mnf designate fluid, SNF, HNF, and MNF. Also, Φ_1 , Φ_2 , and Φ_3 signify the respective solid volume fraction of Al_2O_3 , Cu, and Ni NPs, respectively, while s=3 represents spherical NPs. The experimental value of the Prandtl number utilized for pure water is 6.2, and such value has been widely used by researchers in the existing literature. In the current study, when $\Phi_1 = \Phi_2 = \Phi_3 = 0\%$, the model reduces to conventional third-grade fluid, $\Phi_1 = 5\%$, $\Phi_2 = \Phi_3 = 0\%$ applies to Al_2O_3/H_2O SNF, $\Phi_1 = 5\%$, $\Phi_2 = 5\%$, $\Phi_3 = 0\%$ reduces to Al_2O_3-Cu/H_2O HNF, and

Table 1: The correlations of SNF and HNF [16, 53]

Properties	SNF/HNF
Density	SNF: $\rho_{nf} = (1 - \Phi)\rho_f + \Phi\rho_s$
	$HNF: \rho_{hnf} = [\{(1 - \Phi_1)(1 - \Phi_2)\rho_f\} + \Phi_1\rho_{s1}] + \Phi_2\rho_{s2}$
Heat capacity	$SNF: (\rho \mathcal{C}_p)_{nf} = (1 - \Phi)(\rho \mathcal{C}_p)_f + \Phi(\rho \mathcal{C}_p)_s$
	$HNF: \ (\rho \mathcal{C}_p)_{hnf} = [\{(1-\Phi_1)(1-\Phi_2)(\rho \mathcal{C}_p)_f\} \ + \ \Phi_1(\rho \mathcal{C}_p)_{s1}] \ + \ \Phi_2(\rho \mathcal{C}_p)_{s2}$
Dynamic viscosity	$SNF: \mu_{nf} = rac{\mu_f}{(1-\Phi)^{2.5}}, \ HNF: \mu_{hnf} = rac{\mu_f}{(1-\Phi_1)^{2.5}(1-\Phi_2)^{2.5}}$
Thermal conductivity	$SNF: \; \frac{\kappa_{nf}}{\kappa_{f}} = \left[\frac{\kappa_{S} + (s-1)\kappa_{f} - (s-1)\Phi(\kappa_{f} - \kappa_{S})}{\kappa_{S} + (s-1)\kappa_{f} + \Phi(\kappa_{f} - \kappa_{S})} \right]$
	$HNF: \ \frac{\kappa_{hnf}}{\kappa_{nf}} = \left[\frac{\kappa_{s2} + (s-1)\kappa_{nf} - (s-1)\Phi_2(\kappa_{nf} - \kappa_{s2})}{\kappa_{s2} + (s-1)\kappa_{nf} + \Phi_2(\kappa_{nf} - \kappa_{s2})} \right], \ where$
	$\frac{\kappa_{nf}}{\kappa_{f}} = \left[\frac{\kappa_{S1} + (s-1)\kappa_{f} - (s-1)\Phi_{1}(\kappa_{f} - \kappa_{S1})}{\kappa_{S1} + (s-1)\kappa_{f} + \Phi_{1}(\kappa_{f} - \kappa_{S1})} \right],$

Table 2: MNF relations [29, 30,54]

Poperties	Relations
Density	$\rho_{mnf} = (1 - \Phi_3)([\{(1 - \Phi_1)(1 - \Phi_2)\rho_f\} + \Phi_1\rho_{s1}] + \Phi_2\rho_{s2}) + \Phi_3\rho_{s3}$
Heat	$(\rho C_p)_{mnf} = (1 - \Phi_3)([\{(1 - \Phi_1)(1 - \Phi_2)(\rho C_p)_f\} + \Phi_1(\rho C_p)_{s1}]$
	$+ \Phi_2(\rho C_p)_{52})$
Capacity	$+\Phi_3(ho C_p)_{s3}$
Dynamic viscosity	$\mu_{mnf} = \frac{\mu_f}{(1 - \Phi_1)^{2.5} (1 - \Phi_2)^{2.5} (1 - \Phi_3)^{2.5}}$
Thermal conductivity	$\frac{\kappa_{nf}}{\kappa_{f}} = \left[\frac{\kappa_{S1} + (s-1)\kappa_{f} - (s-1)\Phi_{1}(\kappa_{f} - \kappa_{S1})}{\kappa_{S1} + (s-1)\kappa_{f} + \Phi_{1}(\kappa_{f} - \kappa_{S1})} \right]$
	$\frac{\kappa_{hnf}}{\kappa_{nf}} = \left[\frac{\kappa_{s2} + (s-1)\kappa_{nf} - (s-1)\Phi_{2}(\kappa_{nf} - \kappa_{s2})}{\kappa_{s2} + (s-1)\kappa_{nf} + \Phi_{2}(\kappa_{nf} - \kappa_{s2})} \right]$
	$\frac{\kappa_{mnf}}{\kappa_{hnf}} = \left[\frac{\kappa_{s3} + (s-1)\kappa_{hnf} - (s-1)\Phi_{3}(\kappa_{hnf} - \kappa_{s3})}{\kappa_{s3} + (s-1)\kappa_{hnf} + \Phi_{3}(\kappa_{hnf} - \kappa_{s3})} \right]$

 $\Phi_1 = 5\%$, $\Phi_2 = 5\%$, $\Phi_3 = 9\%$ represents Al₂O₃-Cu-Ni/ H₂O MNF model.

The boundary conditions of the present system is

$$u = u_w(x), \quad v = v_w, \quad -\kappa_{mnf} \frac{\partial T}{\partial y} = h_f(T_w - T),$$

at $y = 0,$ (2.4)
 $u \to u_e(x), \quad \frac{\partial u}{\partial y} \to 0, \quad T \to T_\infty, \text{ as } y \to \infty,$

where v_w represent mass transfer velocity of the wall with $v_w < 0$ for suction and $v_w > 0$ for injection, and h_f is the heat transfer coefficient.

The following transformations are used to make the governing equations non-dimensional as follows [18,52]:

$$\eta = y \sqrt{\frac{u_e(x)}{xv_f}}, \quad u = u_e(x)f'(\eta),$$

$$v = -\sqrt{\frac{u_e(x)v_f}{x}}f(\eta), \quad \theta(\eta) = \frac{T - T_{\infty}}{T_w - T_{\infty}}.$$
(2.5)

In most studies, physical properties of SNF, HNF, and MNF are considered as constants. However, physical features of SNF, HNF, and MNF can fluctuate remarkably with temperature [29,30]. Consequently, to accurately infer the MNF flow and heat transfer rate, it is important to consider temperature-variant MNF viscosity. The variable viscosity for the MNF model is given by [27,28]

Table 3: Transport characteristics for nanomaterials and water [29,30,53]

Thermophysical properties	Regular fluid	Naı	nomaterials	
	H ₂ O	$Al_2O_3(\Phi_1)$	Cu (Ф ₂)	Ni (Φ ₃)
$\rho \text{ (kg m}^{-3})$	997.1	3,970	8,933	8,900
$C_p \; ({\sf J} \; {\sf kg}^{-1} \; {\sf K}^{-1})$	4,179	765	385	444
κ (W m ⁻¹ K ⁻¹)	0.613	40	400	90.7
Pr	6.2	_	-	_

$$\frac{\mu_{mnf}(T)}{\mu_{f}} = \frac{1}{(1 - \Phi_{1})^{2.5}(1 - \Phi_{2})^{2.5}(1 - \Phi_{3})^{2.5}} e^{-\tau(T - T_{\infty})}$$

$$= \frac{\mu_{mnf}}{\mu_{f}} e^{-\tau(T - T_{\infty})} = \frac{\mu_{mnf}}{\mu_{f}} e^{\Lambda\theta},$$
(2.6)

where $\Lambda = -\tau (T_w - T_{\infty})$ is temperature-variant viscosity parameter. By using the aforementioned transformations (2.5) and Eq. (2.6), the governing equations in non-dimensional version is written as follows:

$$\frac{\mu_{mnf}/\mu_{f}}{\rho_{mnf}/\rho_{f}}(f'''e^{\Lambda\theta} + \Lambda f''e^{\Lambda\theta}) + ff'' - f'^{2} + 1$$

$$- \frac{\mu_{mnf}/\mu_{f}}{\rho_{mnf}/\rho_{f}}k_{p}f'e^{\Lambda\theta} + \frac{Z}{\rho_{mnf}/\rho_{f}}e^{-\Omega_{1}\eta}$$

$$+ \frac{\beta_{1}}{\rho_{mnf}/\rho_{f}}(2f'f''' - ff^{iv} + 3f''^{2}) + \frac{2\beta_{2}}{\rho_{mnf}/\rho_{f}}f''^{2}$$

$$+ \frac{6\beta_{3}Re_{x}}{\rho_{mnf}/\rho_{f}}f''^{2}f''' = 0,$$

$$\frac{1}{Pr}\frac{\kappa_{mnf}/\kappa_{f}}{(\rho C_{p})_{mnf}/(\rho C_{p})_{f}}\theta'' + f\theta' + \frac{Q}{(\rho C_{p})_{mnf}/(\rho C_{p})_{f}}\theta$$

$$+ \frac{\mu_{mnf}/\mu_{f}}{(\rho C_{p})_{mnf}/(\rho C_{p})_{f}}Ecf''^{2}e^{\Lambda\theta}$$

$$+ \frac{\beta_{1}Ec}{(\rho C_{p})_{mnf}/(\rho C_{p})_{f}}(f'f''^{2} - ff''f''')$$

$$+ \frac{2\beta_{3}EcRe_{x}}{(\rho C_{n})_{mnf}/(\rho C_{n})_{f}}f''^{4} = 0,$$
(2.8)

with dimensionless inter-related boundary conditions given by

$$f'(0) = \Gamma, \quad f(0) = \lambda, \quad \frac{\kappa_{mnf}}{\kappa_f} \theta'(0) = -\gamma(1 - \theta(0)),$$

$$f'(\eta) \to 1, \quad f''(\eta) \to 0, \quad \theta(\eta) \to 0, \quad \text{as } \eta \to \infty,$$
(2.9)

where $Z=\frac{\pi j_0 M_0}{8a^2 \rho_f}$ is the modified Hartmann number (EMHD parameter); $k_p=\frac{v_f}{ak^*}$ is the porosity parameter; $\beta_1=\frac{a\alpha_1}{\mu_f}$, $\beta_2=\frac{a\alpha_2}{\mu_f}$, and $\beta_3=\frac{a^2\alpha_3}{\mu_f}$ are the material parameters for the third-grade fluid, $\mathrm{Re}_x=\frac{u_w x}{v_f}$ is the local Reynolds number, $\Omega_1=\frac{\pi}{b_1}\sqrt{\frac{v_f}{a}}$ represents the width of the electrodes and magnets, $\mathrm{Ec}=\frac{a^2x^2}{C_p(T_w-T_{co})}$ is the Eckert number, $\mathrm{Pr}=\frac{\mu_f(C_p)_f}{\kappa_f}$ is the Prandtl number, $Q=\frac{Q_0}{a(\rho C_p)_f}$ signifies heat source/sink parameter, and $\gamma=\frac{h_f}{\kappa_f}\sqrt{\frac{v_f}{a}}$, $\Gamma=\frac{u_w}{u_e}$,

and $\lambda = -v_w \sqrt{\frac{x}{u_e v_f}}$ are Biot number, velocity ratio, and mass transpiration parameters, respectively.

2.1 Skin friction, Nusselt number, Sherwood number

The significant physical quantities are the skin friction C_{fx} and local Nusselt number Nu_x , which can be written in the dimensional form as follows:

$$C_{fx} = \frac{\tau_{xy}}{\rho_f u_e^2}, \quad \text{Nu}_x = \frac{xq_w}{\kappa_f (T_w - T_\infty)}, \quad (2.10)$$

where the respective shear stress and heat fluxes near the surface are given by

$$\tau_{xy} = \left[\mu_{mnf}(T) \frac{\partial u}{\partial y} + \alpha_{1} \left(u \frac{\partial^{2} u}{\partial x \partial y} + 2 \frac{\partial u}{\partial x} \frac{\partial u}{\partial y} \right) + v \frac{\partial^{2} u}{\partial y^{2}} \right] + 2\alpha_{3} \left(\frac{\partial u}{\partial y} \right)^{3} \right]_{y=0}, \quad q_{w} \qquad (2.11)$$

$$= -\kappa_{mnf} \left(\frac{\partial T}{\partial y} \right)_{y=0}.$$

Upon the utilization of the transformations in Eq. (2.5), the dimensionless version becomes

$$Re_{x}^{1/2}C_{fx} = \frac{\mu_{mnf}}{\mu_{f}}f''(0)e^{\Lambda\theta(0)} + \beta_{1}(3f'(0)f''(0)$$
$$-f(0)f'''(0)) + 2\beta_{3}Re_{x}[f''(0)]^{3}, \quad (2.12)$$
$$Re_{x}^{-1/2}Nu_{x} = -\frac{k_{mnf}}{\kappa_{f}}\theta'(0).$$

2.2 Entropy generation modelling

Entropy generation of the system is given by [55]

$$Sg''' = \frac{\kappa_{mnf}}{T_{\infty}^{2}} \left(\frac{\partial T}{\partial y}\right)^{2} + \frac{\mu_{mnf}(T)}{T_{\infty}} \left(\frac{\partial u}{\partial y}\right)^{2} + \frac{\alpha_{1}}{T_{\infty}} \left(u\frac{\partial u}{\partial y}\frac{\partial^{2} u}{\partial x \partial y} + v\frac{\partial u}{\partial y}\frac{\partial^{2} u}{\partial y^{2}}\right) + \frac{2\alpha_{3}}{T_{\infty}} \left(\frac{\partial u}{\partial y}\right)^{4} (2.13)$$

By using the similarity transformations and the characteristic entropy generation rate $S_0''' = \frac{\kappa_f a(T_w - T_\infty)}{\nu_f T_\infty}$, the dimensionless entropy generation is written as follows [55]:

$$N_{G} = \frac{S_{g}^{"T}T_{\infty}\nu_{f}}{a\kappa_{f}(T_{w} - T_{\infty})} = \xi_{t}\frac{\kappa_{mnf}}{\kappa_{f}}\theta'^{2} + \operatorname{Br}\frac{\mu_{mnf}}{\mu_{f}}f''^{2}e^{\Lambda\theta} + \beta_{1}\operatorname{Br}(f'f''^{2} - ff''f''') + 2\beta_{3}\operatorname{Re}_{x}\operatorname{Br}f''^{4},$$
(2.14)

where Br = $\frac{\mu_f x^2 a^2}{\kappa_f (T_w - T_\infty)}$ and $\xi_t = \frac{T_w - T_\infty}{T_\infty}$ are Brinkman number and dimensionless temperature difference, respectively.

3 Method of solution

The flow of third-grade fluid model is characterized by strongly nonlinear, coupled, and intricate differential equations because of the non-Newtonian nature of the model. As a result, it becomes very difficult to solve these mathematical equations and obtain solutions that will be more accurate. Most of the time, obtaining closed-form solutions even become impossible. In such situations, we often use the numerical methods to obtain the approximate solutions. Among these numerical methods, we have spectral methods. When collated to approaches such as RK4-method, Keller-Box technique, finite element and difference methods, and spectral methods are mostly preferred because of their remarkable accuracy, convergence, and computational efficacious. Other merits of spectral methods involve their flexibility to be adjusted, so that problems with complicated geometrical configuration and varying types of boundary constraints and those problems with nonlinear nature emanating from extreme nonlinear deformations and materials can be tackled. It has been confirmed in the literature that such good accuracy, convergence, and efficacious vanish when single-domain spectral methods are implemented in larger computational regions. The technique of using more grid points for accuracy improvement also fails and sometimes results in unstable results. The technique of using spectral collocation methods with multiple sub-intervals that are overlapping has been used in some studies [56-60] to alleviate these drawbacks when solving nonlinear differential equations. In all these studies, it was revealed that accuracy, convergence, stability, and computational efficacious become better when spectral collocation methods are used with multi-domain overlapping scheme in both small and large calculation domains. Also, the implementation of the method is quite simple and straightforward, and few grid points and iterations are needed to ensure maximum accuracy and convergence are attained. In view of all the merits of the overlapping grid based spectral collocation methods, more work still needs to be carried out in solving various type of intricate differential equations that are coupled and highly nonlinear. It is very important for these numerical techniques to be well-tested for robustness so that the reader is convinced that they are the most appropriate ones to solve such type of flow problems. In this part of the work, we disclose the overlapping domain decomposition SQLM and its utilization in solving the highly intricate nonlinear coupled ODEs (2.7) and (2.8) that are not amenable to any of the well-known methods. The numerical procedure constitutes the use of multidomain overlapping scheme, quasilinearization method (QLM) [61], spectral collocation method, and univariate Lagrange interpolation polynomials with Chebyshev Gauss-Lobatto grid points [62]. By using the QLM to linearize Eq. (2.7) and (2.8), we obtain

$$\varrho_{4,r}^{(1)}f_{r+1}^{i\nu} + \varrho_{3,r}^{(1)}f_{r+1}^{\prime\prime\prime} + \varrho_{2,r}^{(1)}f_{r+1}^{\prime\prime} + \varrho_{1,r}^{(1)}f_{r+1}^{\prime\prime} + \varrho_{0,r}^{(1)}f_{r+1}
+ \varpi_{0,r}^{(1)}\theta_{r+1} = R_{1,r},$$
(3.1)

$$\varpi_{2,r}^{(2)}\theta_{r+1}'' + \varpi_{1,r}^{(2)}\theta_{r+1}' + \varpi_{0,r}^{(2)}\theta_{r+1} + \varrho_{3,r}^{(2)}f_{r+1}''' + \varrho_{2,r}^{(2)}f_{r+1}'' + \varrho_{1}^{(2)}f_{r+1}'' + \varrho_{0,r}^{(2)}f_{r+1} = R_{2,r},$$
(3.2)

where the coefficients obtained after linearization are provided as follows:

$$\begin{split} \varrho_{4,r}^{(1)} &= -\beta_1 f_r, \, \varrho_{3,r}^{(1)} = G_1 e^{\Lambda\theta_r} + 2\beta_1 f_r' + 6\beta_3 \mathrm{Re}_x f_r''^2, \\ \varrho_{2,r}^{(1)} &= G_1 \Lambda e^{\Lambda\theta_r} + G_2 f_r + 6\beta_1 f_r'' + 4\beta_2 f_r'' \\ &\quad + 12\beta_3 \mathrm{Re}_x f_r'' f_r''', \, \varrho_{1,r}^{(1)} = -G_1 k_p e^{\Lambda\theta_r} + 2\beta_1 f_r''' - 2G_2 f_r', \\ \varrho_{0,r}^{(1)} &= G_2 f_r'' - \beta_1 f_r^{iv}, \\ \varpi_{0,r}^{(1)} &= G_1 \Lambda f_r''' e^{\Lambda\theta_r} + G_1 \Lambda^2 f_r'' e^{\Lambda\theta_r} - G_1 k_p \Lambda f_r' e^{\Lambda\theta_r}, \\ \varpi_{2,r}^{(2)} &= \frac{G_3}{Pr}, \\ \varpi_{2,r}^{(2)} &= G_4 f_r, \\ \varpi_{3,r}^{(2)} &= G_4 f_r, \\ \varrho_{3,r}^{(2)} &= G_1 \mathrm{Ec} f_r f_r'', \, \varrho_{2,r}^{(2)} = 2G_1 \mathrm{Ec} f_r'' e^{\Lambda\theta_r} + 2\beta_1 \mathrm{Ec} f_r' f_r'' \\ &- \beta_1 \mathrm{Ec} f_r f_r''' + 8\beta_3 \mathrm{Ec} \mathrm{Re}_x f_r''^3, \\ \varrho_{1,r}^{(2)} &= \beta_1 \mathrm{Ec} f_r''^2, \, \varrho_{0,r}^{(2)} = G_4 \theta_r' - \beta_1 \mathrm{Ec} f_r'' f_r''', \\ R_{1,r} &= G_1 \Lambda f_r''' \theta_r e^{\Lambda\theta_r} + G_1 \Lambda^2 f_r'' \theta_r e^{\Lambda\theta_r} + G_2 f_r f_r'' \\ &- G_1 k_p \Lambda f_r' \theta_r e^{\Lambda\theta_r} + 2\beta_1 f_r' f_r''' - \beta_1 f_r f_r^{iv} + 3\beta_1 f_r''^2 \\ &+ 2\beta_2 f_r''^2 \\ &+ 12\beta_3 \mathrm{Re}_x f_r''' f_r''^2 - G_2 f_r'^2 - Z e^{-\Omega_1 \eta} - G_2, \\ R_{2,r} &= G_4 f_r \theta_r' + G_1 \mathrm{Ec} f_r''^2 e^{\Lambda\theta_r} + G_1 \Lambda \mathrm{Ec} \theta_r f_r''^2 e^{\Lambda\theta_r} \\ &+ 2\beta_1 \mathrm{Ec} f_r' f_r''^2 - 2\beta_1 \mathrm{Ec} f_r f_r'' f_r''' + 6\beta_3 \mathrm{Ec} \mathrm{Re}_x f_r''^4, \end{split}$$

and $G_1 = \frac{\mu_{mnf}}{\mu_f}$, $G_2 = \frac{\rho_{mnf}}{\rho_f}$, $G_3 = \frac{\kappa_{mnf}}{\kappa_f}$, $G_4 = \frac{(\rho C_p)_{mnf}}{(\rho C_p)_f}$.

To demonstrate the applicability of the overlapping domain decomposition SQLM, we first approximate the original semi-finite domain $[0, \infty)$ with finite region $K = [0, \eta_{\infty}]$. The restricted value η_{∞} is sufficiently big to guarantee that flow features at η_{∞} bear a resemblance to those at ∞ . The truncated domain of concern K is partitioned into \mathcal{E} sub-domains, which are overlapping and designated as follows:

$$K_{\nu} = \left[\eta_0^{\nu}, \eta_{N_{\eta}}^{\nu}\right], \quad \nu = 1, 2, 3, ..., \mathcal{E},$$
 (3.3)

where equal number of Chebyshev collocation points $(N_{\eta}+1)$ are utilized in the discretization of each sub-interval with same length $\mathcal{L}=\frac{\eta_{co}}{\mathcal{E}+(1-\mathcal{E})(1-\cos\frac{\pi}{N_c})/2}$

[56–59]. The diagrammatic representation of how the finite interval is broken down into \mathcal{E} multiple domains is exhibited in Figure 2. From the figure, the initial two quadrature points in the interval $K_{\nu+1}$ are in coincidence with the final two points in the interval K_{ν} , and each corresponding quadrature points are then treated as one grid point.

For the spectral collocation algorithm to be used in the valid interval [-1, 1], the mapping

$$\hat{\eta} = \frac{2}{\eta_{N_n}^{\nu} - \eta_0^{\nu}} \eta - \frac{\eta_{N_n}^{\nu} + \eta_0^{\nu}}{\eta_{N_n}^{\nu} - \eta_0^{\nu}}$$
(3.4)

is used to map the physical coordinate $\eta \in [\eta_0^{\upsilon}, \eta_{N_{\eta}}^{\upsilon}]$ in the interval K_{υ} onto the collocation coordinate $\hat{\eta} \in [-1, 1]$. The collocation points in interval K_{υ} are given in [62] as follows:

$$\{\hat{\eta}_i\}_{i=0}^{N_{\eta}} = \cos\left(\frac{i\pi}{N_{\eta}}\right). \tag{3.5}$$

The unknown function taking $f(\eta)$, for instance, is assumed to be approximated via univariate Lagrange interpolating polynomial in the form

$$f(\eta) \approx F(\eta) = \sum_{i=0}^{N_{\eta}} F(\eta_i) L_i(\eta), \tag{3.6}$$

where $L_i(\eta)$ represents the Lagrange basis polynomials. The corresponding derivatives at the interval $K_v(v=1, 2, 3, ..., \mathcal{E})$ are approximated at the collocation points $\hat{\eta}_i$, $j=0, 1, 2, ..., N_n$ as follows:

$$\frac{\mathrm{d}f}{\mathrm{d}\eta} \approx \sum_{i=0}^{N_{\eta}} F(\eta_i) L_i'(\eta_j) = \sum_{j=0}^{N_{\eta}} \mathbf{D}_{i,j}^{\nu} F(\eta_j) = \mathbf{D}\mathbf{F}, \qquad (3.7)$$

where $\hat{\mathbf{D}} = \left(\frac{2}{\mathcal{L}}\right)\hat{\mathbf{D}}$ is the differential matrix on the interval K_v and $\hat{\mathbf{D}}$ is the standard first order Chebyshev differential matrix with order $(N_\eta + 1) \times (N_\eta + 1)$ [62,63]. The matrix-vector \mathbf{F} is given by

$$\mathbf{F} = [f(\eta_0^{\nu}), f(\eta_1^{\nu}), \dots, f(\eta_N^{\nu})]^{\mathrm{T}}, \tag{3.8}$$

where the capital letter T stands for the matrix transpose. With regard to the aforestated properties of the overlapping domain decomposition technique, the arrangement of the differential matrix **D** having order $(N_t + 1) \times (N_t + 1)$ with $N_t = N_\eta + (N_\eta - 1) \times (\mathcal{E} - 1)$ is given by

where the rest of the components in the matrix \mathbf{D} are zeros. The nth order space derivative for the function f in the overall domain is approximated as follows:

$$\frac{\mathrm{d}^n f}{\mathrm{d}\eta^n} \approx \mathbf{D}^n \hat{\mathbf{F}},\tag{3.10}$$

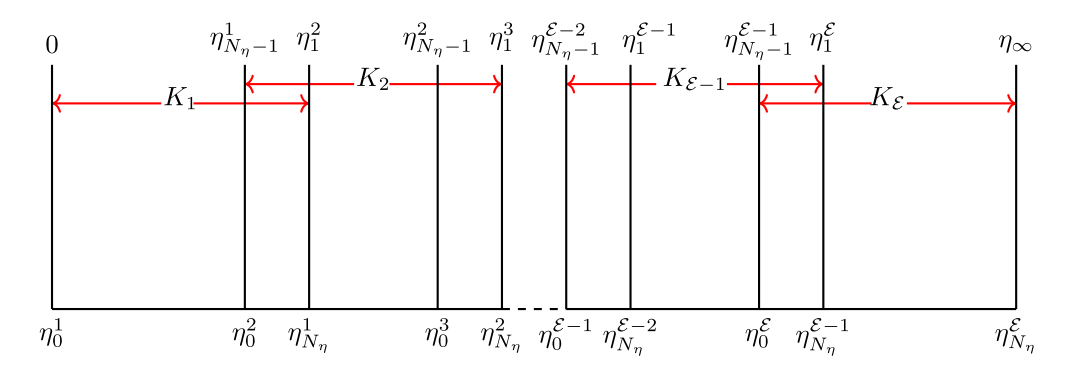


Figure 2: Overlapping domain decomposition of $[0, \eta_{-1}]$.

where the new matrix-vector $\hat{\mathbf{F}}$ symbolizing the solution across all sub-intervals is given as follows:

$$\hat{\mathbf{F}} = [f(\eta_0), f(\eta_1), ..., f(\eta_N)]^{\mathrm{T}}.$$
 (3.11)

The similar procedure is used to approximate the other functions along with their derivatives. Upon the execution of spectral collocation procedure and the use of discrete derivatives in Eq. (3.1) and (3.2), we have the following matrix equations:

$$[\boldsymbol{\varrho}_{4,r}^{(1)}\mathbf{D}^{4} + \boldsymbol{\varrho}_{3,r}^{(1)}\mathbf{D}^{3} + \boldsymbol{\varrho}_{2,r}^{(1)}\mathbf{D}^{2} + \boldsymbol{\varrho}_{1,r}^{(1)}\mathbf{D} + \boldsymbol{\varrho}_{0,r}^{(1)}]\hat{\mathbf{F}} + [\boldsymbol{\varpi}_{0,r}^{(1)}]\hat{\boldsymbol{\theta}} = \mathbf{R}_{1,r},$$
(3.12)

$$[\boldsymbol{\varpi}_{2,r}^{(2)} \mathbf{D}^{2} + \boldsymbol{\varpi}_{1,r}^{(2)} \mathbf{D} + \boldsymbol{\varpi}_{0,r}^{(2)}] \hat{\boldsymbol{\Theta}} + [\boldsymbol{\varrho}_{3,r}^{(2)} \mathbf{D}^{3} + \boldsymbol{\varrho}_{2,r}^{(2)} \mathbf{D}^{2} + \boldsymbol{\varrho}_{1,r}^{(2)} \mathbf{D} + \boldsymbol{\varrho}_{0,r}^{(2)}] \hat{\mathbf{F}} = \mathbf{R}_{2,r}.$$
(3.13)

Equations (3.12) and (3.13) comprise an $2(N_t + 1) \times 2(N_t + 1)$ matrix system presented in the form

$$\begin{bmatrix} \mathbf{A}_{1,1} & \mathbf{A}_{1,2} \\ \mathbf{A}_{2,1} & \mathbf{A}_{2,2} \end{bmatrix} \begin{bmatrix} \hat{\mathbf{r}} \\ \hat{\boldsymbol{\theta}} \end{bmatrix} = \begin{bmatrix} \mathbf{R}_1 \\ \mathbf{R}_2 \end{bmatrix}$$
(3.14)

or

$$\mathbf{\Delta}_r \mathbf{B}_{r+1} = \mathbf{H}_r. \tag{3.15}$$

The boundary conditions are imposed on the main diagonal sub-matrices in the matrix system (3.15) to obtain a new system which is then solved iteratively to attain the numerical solutions concurrently across the entire multiple domains. The following initial assumptions complying with the boundary conditions are chosen to initiate the iteration process:

$$f_0(\eta) = \Gamma(1 - e^{-\eta}) + e^{-\eta} + \eta - 1 + \lambda, \, \theta_0(\eta)$$

$$= \frac{\gamma}{1 + \nu} e^{-\eta \frac{k_f}{k_{mnf}}}.$$
(3.16)

3.1 Error bound in the overlapping domain decomposition scheme

In this subsection of the work, the univariate polynomial interpolation error bound theorem for the single fixed domain given in ref. [60] is being extended to be applicable in subdivided domain. We remark that the number of C-G-L nodes is presumed to be fixed for all subdomains.

Theorem 1. The error bound when the C-G-L points $\{\eta_i\}_{i=0}^{N_{\eta}} \in [\eta_0^{\upsilon}, \eta_N^{\upsilon}], \upsilon = 1, 2, 3, ..., \mathcal{E}, in the partitioned vari$ able η are employed in the interpolation via univariate polynomial is provided as follows:

$$E(\eta) \le \frac{4}{2^{N_{\eta}}(N_{\eta}+1)!} \left(\frac{\mathcal{L}}{2}\right)^{N_{\eta}+1} f^{(N_{\eta}+1)}(\Upsilon_{\eta}), \qquad (3.17)$$

where Y_n is the error function.

Proof of Theorem 1. Throughout the calculation domain $[0, \eta_{\infty}]$, it holds that

$$\left| \prod_{j=0}^{N_{\eta}} (\eta - \eta_i) \right| \leq \frac{4}{2^{N_{\eta}}} \left(\frac{\eta_{\infty}}{2} \right)^{N_{\eta}+1}, \eta \in [0, \eta_{\infty}]. \quad (3.18)$$

This suggests that within each sub-interval in the divided domain, we ought to have

$$\left| \prod_{i=0}^{N_{\eta}} (\eta - \eta_{i}) \right| \leq \frac{4}{2^{N_{\eta}}} \left(\frac{\mathcal{L}}{2} \right)^{N_{\eta}+1}, \, \eta \in \left[\eta_{0}^{\upsilon}, \, \eta_{N_{\eta}}^{\upsilon} \right], \quad (3.19)$$

$$\upsilon = 1, 2, 3, \dots, \mathcal{E}.$$

If $f(\eta)$ is a smooth function, then $\exists Y_l \in [\eta_0^l, \eta_{N_n}^l], l =$ (3.16) 1, 2, 3, ..., \mathcal{P} , such that the value of $f^{(N_{\eta}+1)}(Y_l)$ is the absolute extrema of $f^{(N_{\eta}+1)}(\eta)$ in $[\eta_0^l, \eta_{N_{\eta}}^l]$. Owing to such, the error bound can be expressed in form of elements within each sub-interval as follows:

$$\left\{ \frac{4}{2^{N_{\eta}}(N_{\eta}+1)!} \left(\frac{\mathcal{L}}{2} \right)^{N_{\eta}+1} f^{(N_{\eta}+1)}(Y_{l}) \right\}_{l=1}^{\mathcal{E}}.$$
 (3.20)

We provide

$$\|\hat{f}^{(N_{\eta}+1)}(Y)\|_{\infty}$$

$$\equiv \max\{f^{(N_{\eta}+1)}(Y_{1}), f^{(N_{\eta}+1)}(Y_{2}), f^{(N_{\eta}+1)}(Y_{3}), \dots, (3.21)\}$$

$$f^{(N_{\eta}+1)}(Y_{\mathcal{E}})\},$$

to designate the maximum absolute value of $f(\eta)$ when differentiated $(N_{\eta}+1)$ times with respect to η in the calculation domain $[0,\eta_{\infty}]$. Assuredly, $\|\hat{f}^{(N_{\eta}+1)}(\Upsilon)\|_{\infty} = f^{(N_{\eta}+1)}(\Upsilon_{\eta})$. To stretch the error bound throughout the calculation domain, it is necessary to consider the greatest possible error across the entire sub-intervals given as follows:

$$\frac{4}{2^{N_{\eta}}(N_{\eta}+1)!} \left(\frac{\mathcal{L}}{2}\right)^{N_{\eta}+1} f^{(N_{\eta}+1)}(Y_{\eta}). \tag{3.22}$$

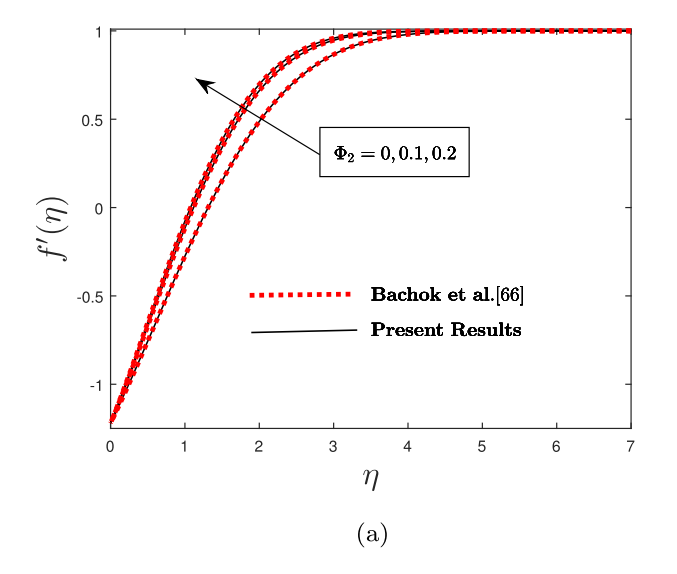
Through the use of Eq. (3.22) and $||f(\eta) - F(\eta)|| \le \frac{1}{(N_{\eta}+1)} f^{(N_{\eta}+1)}(\Upsilon_{\eta}) \prod_{i=0}^{N_{\eta}} (\eta - \eta_i)$ [60], where $F(\eta)$ is an $(N_{\eta}+1)^{\text{th}}$ order interpolating polynomial for approximating $f(\eta)$, the proof is complete.

From Eq. (3.17), it is evident that the error in univariate polynomial interpolation is substantially smaller when interpolation is carried out on partitioned

domain than on a single fixed domain. This is because $\left(\frac{\mathcal{L}}{2}\right)^{N_\eta+1} \ll \left(\frac{\eta_\infty}{2}\right)^{N_\eta+1}$ for large \mathcal{E} , which in turn lead to reduction in the size of the interpolation error.

4 Computed results and discussion

This part of the work gives a detailed account of the numerical results obtained through solving the transmuted nonlinear coupled ODEs using SOLM via the overlapping grid scheme. The numerical solutions are attained for varying values of governing parameters to disclose their significant effect on flow variables, quantities of engineering concern and entropy production. The chosen values of the flow parameters are $\Lambda = 0.4$, $k_p = 0.5$, $\beta_1 = 0.1$, $\beta_2 = 0.1$, $\beta_3 = 0.1$, $Re_x = 0.2$, Z = 0.1, $\Omega_1 = 0.1$, Q = 0.5, Ec = 0.1, Pr = 6.2, $\Gamma = 0.2$, $\lambda = 2$, and y = 0.5. The graphs and tables were prepared using N_{η} = 30 and \mathcal{E} = 4. All these parameter values were considered the same in the whole study, unless stated. We have also replaced the semi-finite domain of the problem $[0, \infty)$ with finite computational domain [0, 2], since for any $\eta > 2$, there is an insignificant change in the numerical results. To approve the choice of the method and the inspected model, our numerical results are matched with findings from previous studies by Wang [64], Bachok et al. [65], and Yacob et al. [66] for the limiting case in Figure 3 and Tables 4 and 5. It is interesting to note that



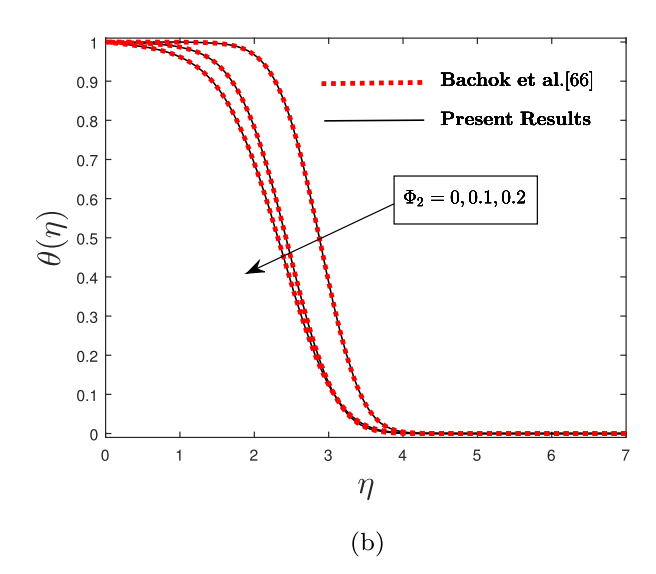


Figure 3: Comparison of the present results of flow profiles with Bachok *et al.* [65] for Cu/H₂O SNF. (a) Velocity fields against different $\Phi_2(\Phi_1 = \Phi_3 = 0)$ and (b) temperature fields against different $\Phi_2(\Phi_1 = \Phi_3 = 0)$.

Table 4: Numerical values of f''(0) for different Γ and Φ_2 (Cu/H₂O SNF) when $\Phi_1 = \Phi_3 = 0$

Г	Wang [64]		Bachok et al. [65]		Present results	
	$\Phi_2 = 0$	$\Phi_2 = 0$	$\Phi_2 = 0.1$	$\Phi_2 = 0.2$	$\Phi_2 = 0$	$\Phi_2 = 0.1$	$\Phi_2 = 0.2$
2	-1.88731	-1.887307	-2.217106	-2.298822	-1.8873066	-2.2171059	-2.2988221
0.5	0.71330	0.713295	0.837940	0.868824	0.7132946	0.8379403	0.8688244
0	1.232588	1.232588	1.447977	1.501346	1.2325878	1.4479773	1.5013457
-0.5	1.49567	1.495670	1.757032	1.821791	1.4956698	1.7570319	1.8217912
-1	1.32882	1.328817	1.561022	1.618557	1.3288169	1.5610225	1.6185570

validation of the code is done for both conventional fluid and SNF models (Cu/H₂O and Al₂O₃/H₂O). The sets of results demonstrate coherent agreement; thus, the utilized method is confirmed to be reliable and the proposed MNF model is validated.

Tables 6 and 7 and Figure 4 are provided to justify the choice of overlapping grid SQLM scheme over the usual single-domain SQLM. Table 5 shows that the overlapping domain decomposition approach is remarkably accurate in both small and large computational domains. This claim is confirmed by very small residual error estimates and condition numbers in the column of overlapping SQLM than in the column of the usual single domain SQLM. Since η_{∞} = 2 in the current problem is considered big enough to guarantee that flow features at this value bear a resemblance to those at infinity, Table 6 approves the overlapping grid SQLM as a preferred method to ensure maximum accuracy in the domain [0, 2]. Table 6 also indicates that errors and condition numbers reduce drastically when the computational domain is being stretched from small to large. This indicates that the accuracy improves when the computational domain is stretched in the overlapping domain decomposition scheme. This finding is in concurrence with the error bound given in Eq. (3.17), where increment in the length of sub-intervals is proven to contribute towards the reduction of the interpolation error. Table 7 elucidates that residual error values, execution times, and condition numbers for the coefficient matrix Δ are clearly smaller in the multi-domain SQLM with overlapping scheme than in the single-domain SQLM. Also, the accuracy, computational effectiveness, and stability are improved by considering few grid points within a subinterval while increasing the number of multiple domains. This is demonstrated by the reduction in residual error values, runtime, and condition numbers as collocation nodes within each sub-interval are decreased, concurrently increasing the number of multiple domains. The location and the number of non-zero elements in the coefficient matrix Δ are demonstrated in Figure 4. By using the overlapping domain decomposition scheme and further

Table 5: Numerical values of coefficient of skin friction and thermal rate for Al_2O_3/H_2O SNF ($\Phi_2 = \Phi_3 = 0$) and Cu/H_2O SNF ($\Phi_1 = \Phi_3 = 0$) when Φ_1 and Φ_2 are varied

		Yacob et al. [66]	Bachok e	t al. [65]		Present results	
$\mathbf{\Phi}_1$	Γ	$\frac{\mu_{mnf}}{\mu_f}f''(0)$	$-\frac{k_{mnf}}{k_f}\boldsymbol{\theta'}(0)$	$\frac{\mu_{mnf}}{\mu_f}f''(0)$	$-\frac{k_{mnf}}{k_f}\boldsymbol{\theta'}(0)$	$\frac{\mu_{mnf}}{\mu_f}f''(0)$	$-\frac{k_{mnf}}{k_f}\boldsymbol{\theta'}(0)$
0.1	-0.5	_	_	1.9440	0.7272	1.9439980	0.7271485
0.2	-0.5	_	_	2.4976	0.8878	2.4976510	0.8878485
0.1	0	1.6019	1.3305	1.6019	1.3305	1.6020567	1.3305085
0.2	0	2.0584	1.5352	2.0584	1.5351	2.0583239	1.5351604
0.1	0.5	_	_	0.9271	1.8278	0.9271059	1.8278469
0.2	0.5	_	_	1.1912	2.0700	1.1911467	2.0699869
Φ ₂	Γ	$\frac{\mu_{mnf}}{\mu_f}f''(0)$	$-\frac{k_{mnf}}{k_f}\theta'(0)$	$\frac{\mu_{mnf}}{\mu_f}f''(0)$	$-\frac{k_{mnf}}{k_f}\theta'(0)$	$\frac{\mu_{mnf}}{\mu_f}f''(0)$	$-\frac{k_{mnf}}{k_f}\theta'(0)$
0.1	-0.5	_	_	2.2865	0.8385	2.2865115	0.8385102
0.2	-0.5	_	_	3.1826	1.0802	3.1825388	1.0803080
0.1	0	1.8843	1.4043	1.8843	1.4043	1.8843238	1.4043271
0.2	0	2.6226	1.6692	2.6226	1.6692	2.6227434	1.6693377
0.1	0.5	_	_	1.0904	1.8724	1.0904524	1.8723864
0.2	0.5	_	_	1.5177	2.1577	1.5177739	2.1576903

Table 6: Condition numbers and residual error values when the size of domains is varied

	$N_l = N_{\eta} = 120$,	$\mathcal{E}=1$		$N_{\eta}=2(N_{l}=61),$	<i>E</i> = 60	
$[0,\eta_{\infty}]$	$\ Res(f)\ _{\infty}$	$\ Res(\boldsymbol{\theta})\ _{\infty}$	Cond (Δ)	$\ Res(f)\ _{\infty}$	$\ Res(\boldsymbol{\theta})\ _{\infty}$	Cond (Δ)
[0, 1]	5.446182×10^{-3}	2.75180×10^{-5}	6.08686×10^{14}	1.348238 × 10 ⁻⁹	1.62534×10^{-11}	3.84057×10^7
[0, 2]	3.435438×10^{-4}	2.05298×10^{-6}	5.50742×10^{13}	1.241761×10^{-10}	1.14733×10^{-12}	3.39504×10^{6}
[0, 4]	1.085894×10^{-4}	2.76485×10^{-7}	6.03703×10^{12}	3.521036×10^{-11}	3.02845×10^{-13}	3.70238×10^{5}
[0,8]	1.430288×10^{-6}	2.68188×10^{-8}	8.20196×10^{11}	3.367279×10^{-12}	2.04663×10^{-14}	5.56446×10^4
[0, 12]	1.430288×10^{-6}	2.68188×10^{-8}	8.20196×10^{11}	2.507133×10^{-12}	6.62317×10^{-15}	2.40898×10^4
[0, 16]	6.185510×10^{-7}	2.07301×10^{-9}	1.41444×10^{11}	1.849854×10^{-12}	7.33831×10^{-15}	1.55597×10^{4}
[0, 20]	1.535048×10^{-6}	1.16860×10^{-9}	8.38888×10^{10}	9.347627×10^{-13}	2.39609×10^{-15}	1.20519×10^{4}
[0, 26]	5.825402×10^{-7}	4.19018×10^{-10}	5.54015×10^{10}	9.111947×10^{-13}	1.02414×10^{-15}	9.65948×10^{3}
[0, 30]	3.862862×10^{-7}	2.14969×10^{-10}	3.37522×10^{10}	9.560165×10^{-13}	8.27938×10^{-16}	8.82996×10^{3}

increasing the number of sub-domains, the matrices emerging in the implementation of the spectral collocation method are sparse since the matrix contains mostly zero components when compared to the single-domain SQLM. This very small sparse matrix helps to ensure stability in the system and minimize the computational storage better than in the usual single-domain approach. Thus, computation of the inverse of such matrix when solving the resulting matrix system iteratively is possible with minimal numerical errors and good approximation accuracy.

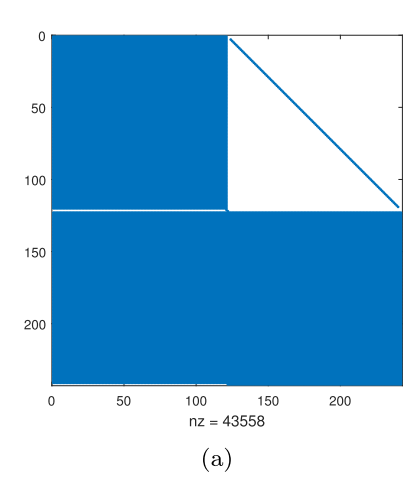
Figure 5 elucidates how the graphs for residual errors and solution errors behave when the number of iterations are increased in the iteration process. Both graphs depicts a monotonic reduction with regard to iterations increment, and this behaviour implies convergence of the method. When the graphs begin to demonstrate little or no decline, then full convergence is reached. The accurateness of the method is also demonstrated by the little residual error estimates after the convergence is reached.

To obtain a clear awareness of the physics of the flow problem, variations of entropy, velocity, and temperature profiles against different controlling parameters are

disclosed in Figures 6-17. All figures have been plotted for $\Gamma = -0.5$ (shrinking sheet) and $\Gamma = 0.2$ (stretching sheet). In the case of the stretching sheet, the profiles of velocity $f'(\eta)$ are always positive and asymptotically approach 1 as η becomes large $(\eta \to \infty)$. This implies that the velocity component of the fluid, u = axf' always takes positive values since a > 0; thus, the fluid disseminate along with the plate at all points. However, for the case shrinking, the profiles of velocity are negative near the surface, but after some value of $\eta(\eta \approx 0.2)$ away from the surface, the profiles become positive throughout the entire flow regime while asymptotically approaching 1. This suggest that the fluid near the surface moves along with the shrinking plate and the fluid away from the surface disseminate in the opposite direction. On the other hand, temperature and entropy generation curves are higher in the shrinking case than in the stretching case. This is because the thermal boundary layer of the shrinking Riga surface is thicker than the stretching Riga surface. The less entropy generated with large Γ is subject to the condition that velocity near the surface is less than that of the free stream velocity. It is also perceived that both profiles of velocity

Table 7: Condition numbers, residual error values, and execution time when N_n and \mathcal{E} are varied

N _η	3	$\ Res(f)\ _{\infty}$	$\ Res(oldsymbol{ heta})\ _{\infty}$	Cond (Δ)	Runtime (s)
120	1	3.862862×10^{-7}	2.14969×10^{-10}	3.37522 × 10 ¹⁰	0.389483
60	2	1.879395×10^{-7}	2.08051×10^{-11}	1.88496×10^9	0.317371
40	3	2.148450×10^{-8}	4.34984×10^{-12}	3.62020×10^{8}	0.291249
30	4	9.799008×10^{-9}	8.37306×10^{-12}	1.22806×10^{8}	0.223130
15	8	4.771338×10^{-10}	4.66446×10^{-13}	9.58493×10^{6}	0.215285
8	15	7.061280×10^{-11}	9.25581×10^{-14}	1.15954×10^6	0.193218
4	30	1.619262×10^{-11}	8.98347×10^{-15}	1.69459×10^{5}	0.158996
3	40	4.652243×10^{-12}	4.32553×10^{-15}	6.25561×10^4	0.117933
2	60	9.560165×10^{-13}	8.27938×10^{-16}	8.82996×10^{3}	0.071437



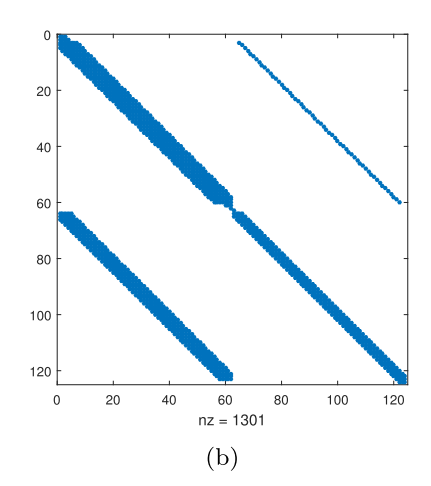
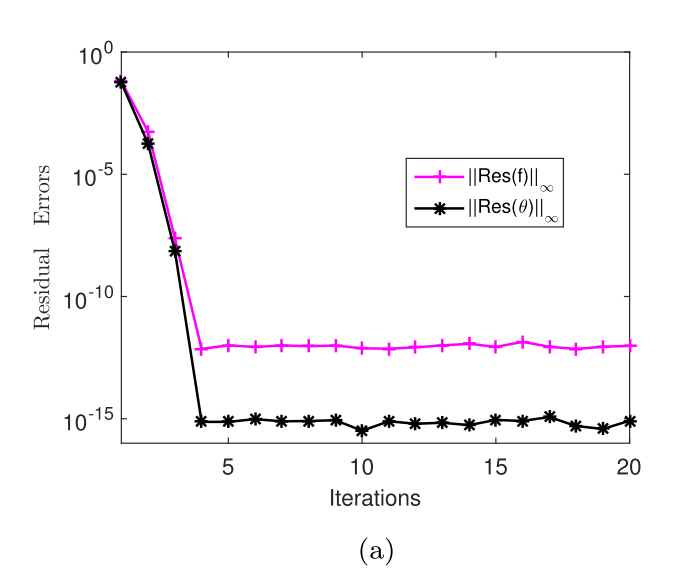


Figure 4: Sparseness arrangement of coefficient matrix Δ for varying N_{η} and \mathcal{E} . (a) Single-domain SQLM ($N_{\eta} = 120$, $\mathcal{E} = 1$) and (b) overlapping grid SQLM when $N_{\eta} = 2$, $\mathcal{E} = 60$.

and temperature satisfy the imposed boundary conditions asymptotically, thus justifying the authentication of the computed numerical results. Figure 6 demonstrates velocity curves when varying the types of fluids and volume fraction of Ni NPs. It is clear in Figure 6(a) that high magnitude of velocity belongs to the case of MNF, whereas the lowest magnitude of velocity correspond to the case of conventional third-grade fluid for both stretching and shrinking surfaces. This shows that the velocity of MNF upsurges quickly than that of the third-grade fluid. Physically, the dispersion of NPs changes thermo-physical properties of the fluid, thus contributing towards extra thinning of the thickness of hydrodynamic boundary layer and massive increment in the velocity field. These interesting results are in accordance with findings reported by Khashi'ie

et al. [18] and Siddique et al. [19] in the case of second-grade HNF model. A similar observation is noted in Figure 6(b) when $\Gamma=-0.5$ and $\Gamma=0.2$, where the curves attain maximum velocity with the increment of Ni NPs from 0 to 9% since the thermal conductivity of the fluid is directly proportional to the solid volume fraction. The case of $\Phi_3=0\%$ signifies the HNF model (i.e., Ni NPs are absent) with lower velocity than MNF model. As Ni NPs are added, kinetic energy is accelerated within the fluid particles, which improves the collision of base fluid and NPs. Thus, large Φ_3 boosts the potential of heat transmission (thermal expansion), and upsurge in fluid motion is expected, leading to a rise in MNF velocity.

Figure 7 illustrates the variation of temperature profiles with different types of fluids and volume fractions of



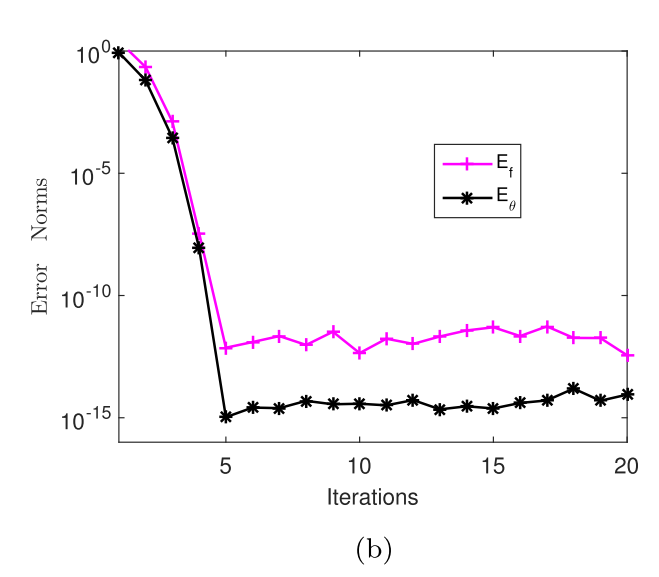


Figure 5: Behaviour of (a) residual errors (b) and error norms against iterations when $N_q=2$ and $\mathcal{E}=60$.

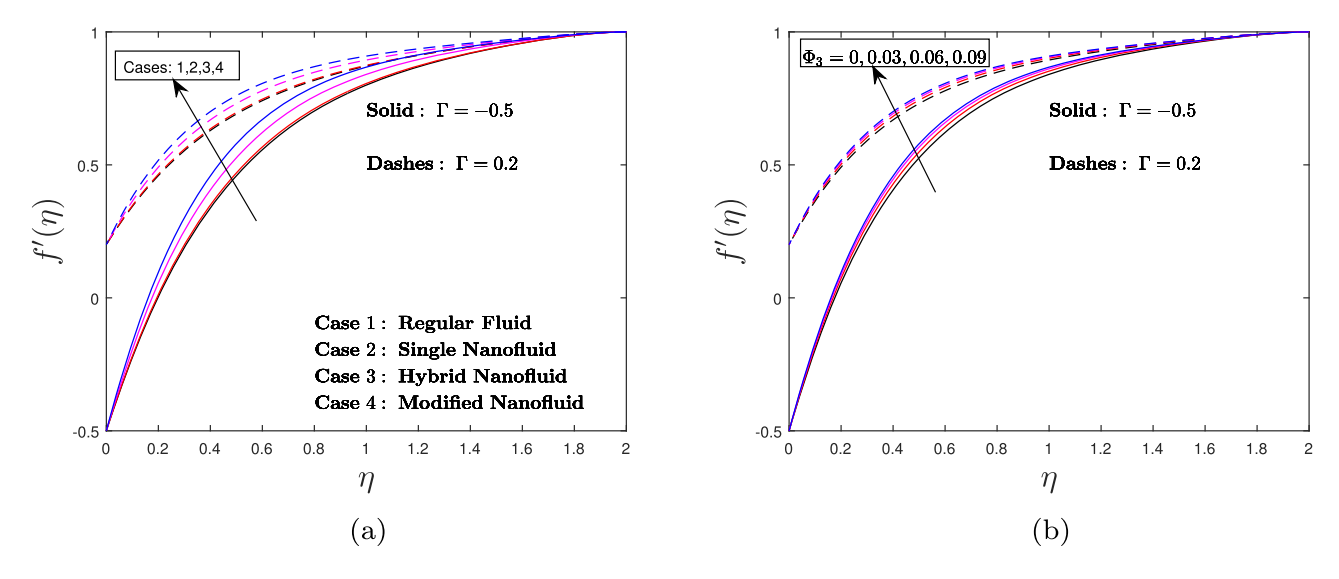


Figure 6: Behaviour of (a) regular fluid, SNF, HNF, MNF, and (b) Φ_3 on velocity fields.

Ni NPs. In both stretching and shrinking Riga plate, Figure 7a shows that higher temperature relates to MNF, while lower temperature belongs to the conventional third-grade fluid. This is because of the improvement in thermal conductivity from the base fluid to SNF, then from SNF to the HNF, and finally from HNF to the MNF. The concentration of NPs is augmented because of direct influence of thermal conductivity on concentration of NPs. From physical perspective, energy in the form of heat is distributed from NPs; thus, incorporation of more different kinds of NPs (MNF model) can make use of more energy, which in turn amplifies the temperature along with thickness of the thermal boundary layer. As expected in Figure 7b, the profiles of temperature and thermal boundary layer thickness accelerate with

increment in the values of solid volume fraction of nickel (Φ_3) for the MNF model. The rise in Φ_3 implies enhancement of the concentration within the resultant nanofluid and more availability of space for intensification in heat conduction. Thus, the addition of more Ni NPs exerts more energy that causes heat dispersion within the surface, consequently boosting thermal boundary layer thickness and MNF temperature. These results verify that desirable thermal augmentation, particularly near the surface, can be achieved through using the Al_2O_3 -Cu-Ni/ H_2O MNF model with more Ni NPs. The high velocity and temperature associated with MNF implies that modified hybrid technology can assist in enhancing the physical attributes of the fluid with minimal cost effects.

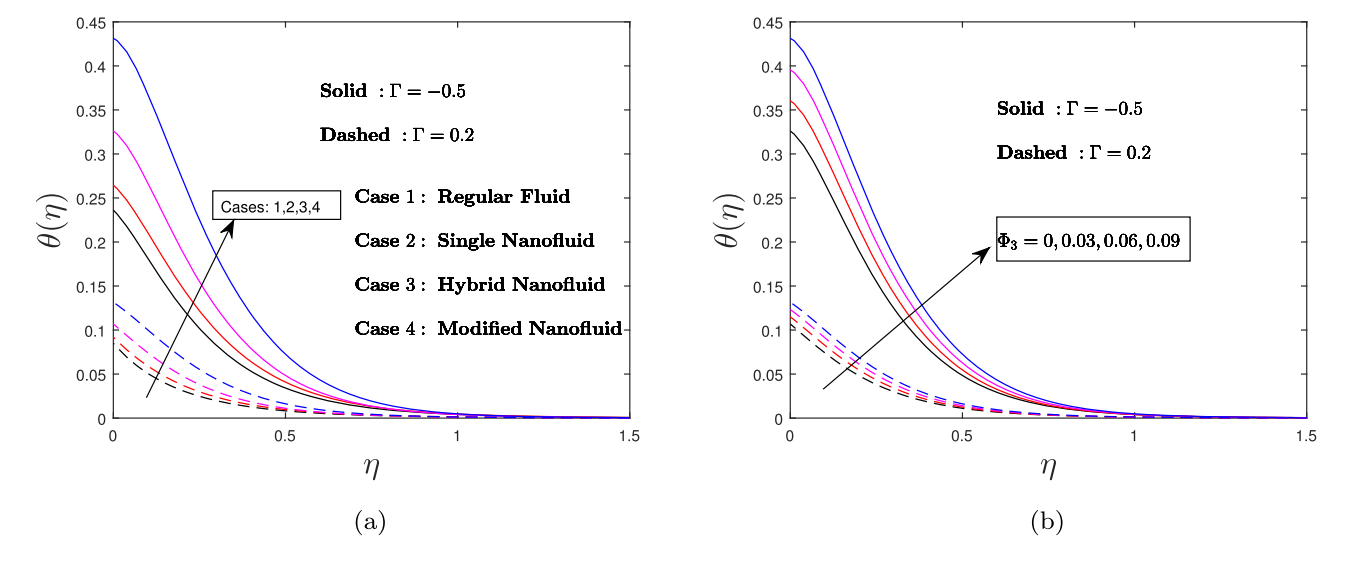
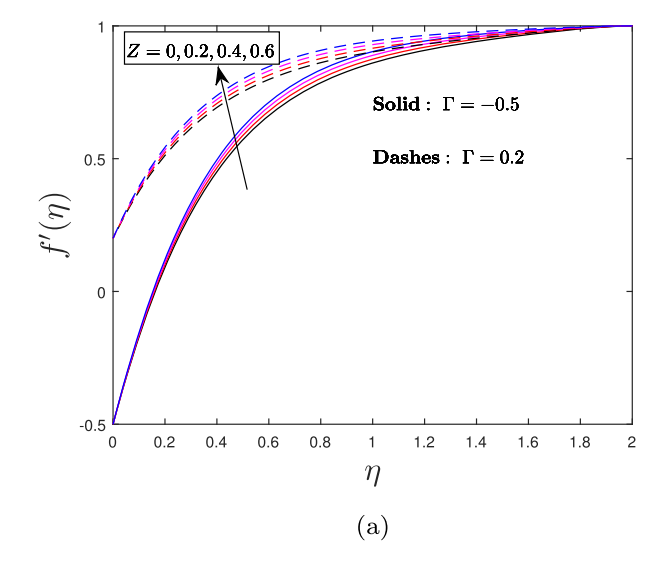


Figure 7: Behaviour of (a) regular fluid, SNF, HNF, MNF, and (b) Φ_3 on thermal fields.



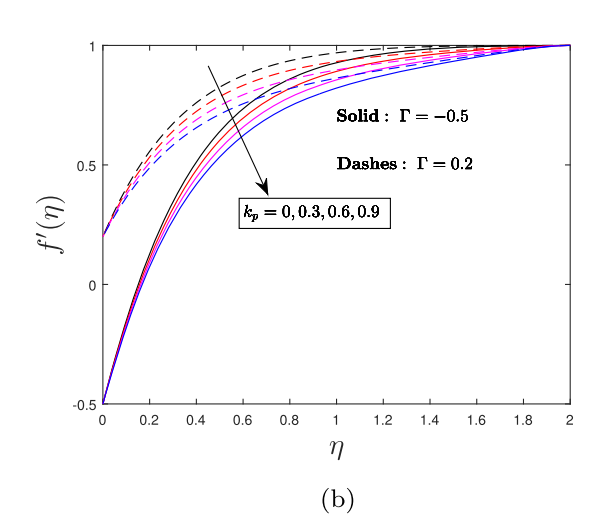
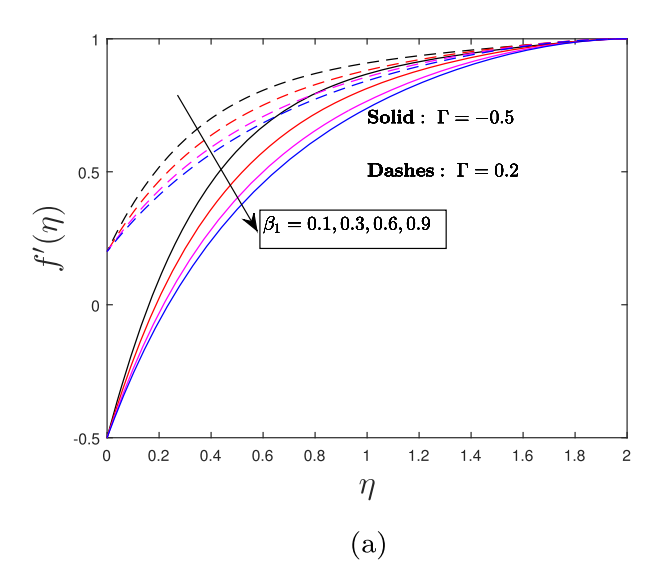


Figure 8: Velocity fields against different (a) Z and (b) k_p .

From Figure 8a, the increment in the velocity gradient causes the momentum boundary layer to become slightly thinner with increment in the modified Hartman number (Z); thus, MNF velocity is perceived to improve for both cases of stretching and shrinking surface. This upsurge of velocity curves is a clear indication that the fluid velocity closer to the surface surpasses the fluid velocity at the free stream. From the physical point of view, large values of Z ascertain the intensity of external electric field that assists flow of the fluid, accordingly Lorentz force is activated. The existence of Lorentz forces possesses the separation of laminar boundary layer flow that gently aid the movement of third-grade MNF NPs, thereby leading to enhancement in velocity. The impact

of the porosity parameter k_p on the velocity profiles is highlighted in Figure 8b when $\Gamma=-0.5$ and $\Gamma=0.2$. For both cases of Γ , the velocity drops with increment in k_p , which is responsible for higher fluid viscosity that produces resistance between fluid particles. From the physical perspective, the void spaces within the medium upsurge with large values of k_p , which give additional resistive forces to the motion of the fluid. Thus, the flow of the fluid is decelerated leading to a decrement in the third-grade MNF velocity.

Figure 9 portrays the outcome of varying the thirdgrade parameter (β_1) on the velocity and temperature fields. Figure 9a demonstrates that the velocity of the MNF declines with large values of β_1 for both stretching



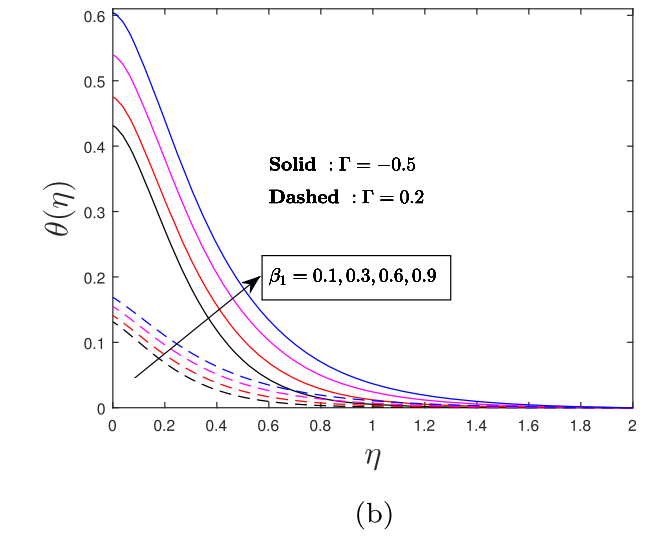


Figure 9: (a) Velocity and (b) thermal fields against different β_1 .

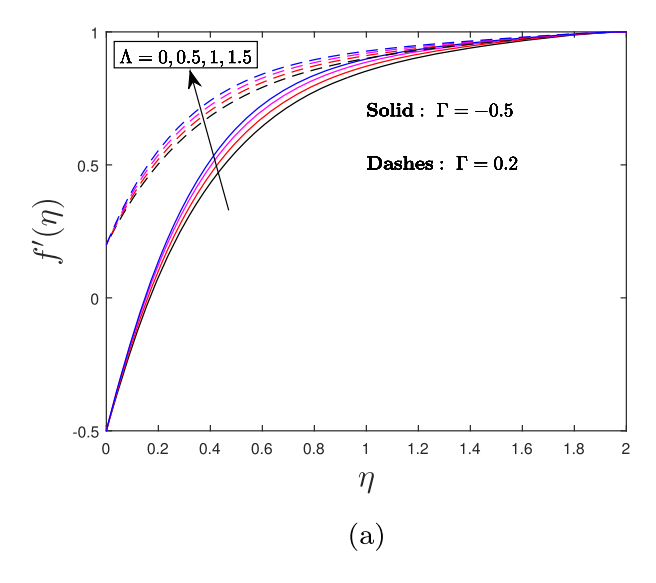


Figure 10: (a) Velocity and (b) thermal fields against different Λ .

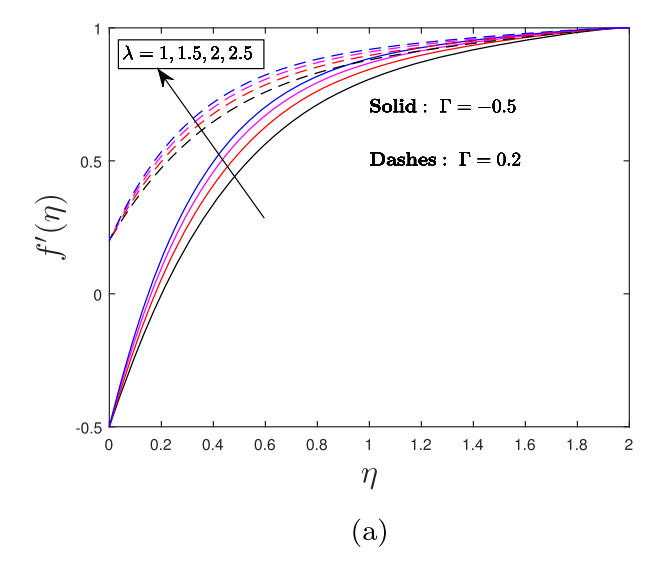
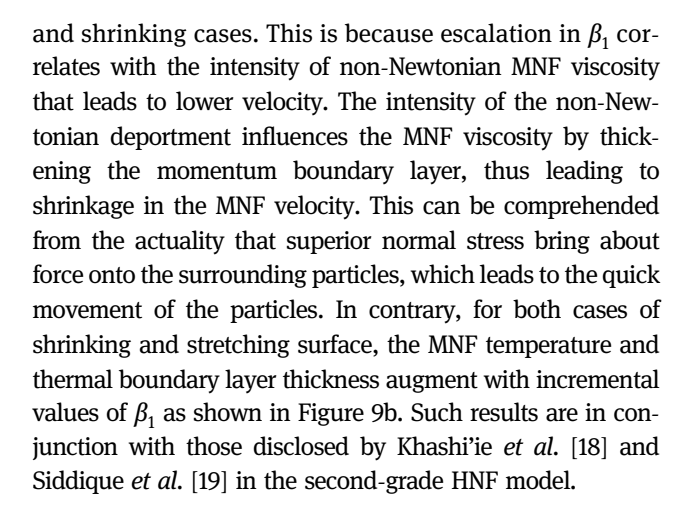
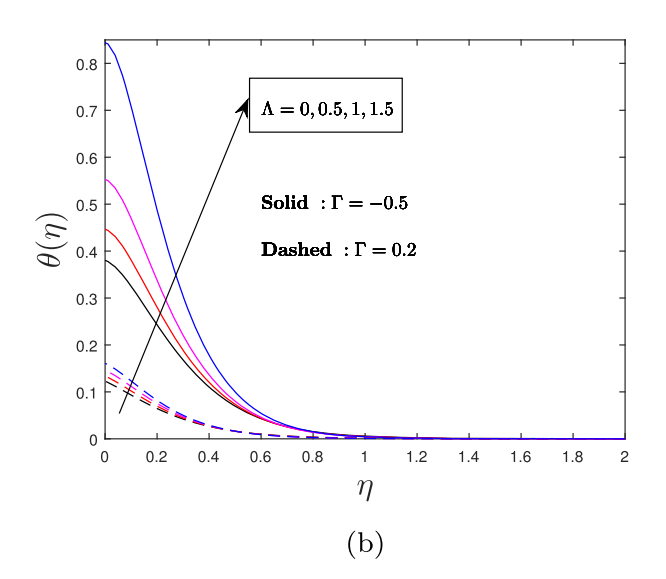


Figure 11: (a) Velocity and (b) thermal fields against different λ .





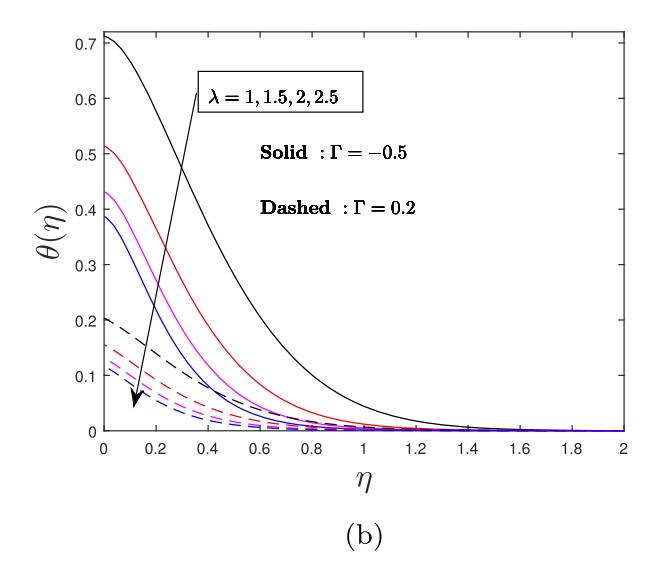
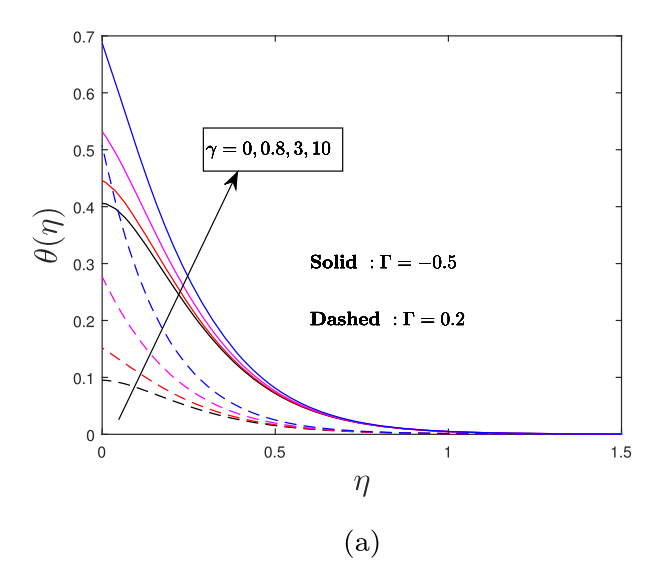


Figure 10 elucidates the impact of fluid variable physical properties on both velocity and temperature distributions. In both cases of stretching and shrinking Riga plate, it is clear that increment in the viscosity variant parameter leads to augmentation in the non-dimensional flow and temperature. This is due to the fact that an increase in the variable viscosity parameter has a potential of increasing the temperature difference $(T_w - T_{\infty})$, thus weakening the third-grade fluid bond and minimizing the strength of dynamic viscosity of the non-Newtonian fluid. Thus, both velocity and thermal boundary layer thicknesses are improved, leading to upsurge in MNF velocity and temperature. Figure 11 stipulates the repercussions of suction parameter $(\lambda > 0)$ on both



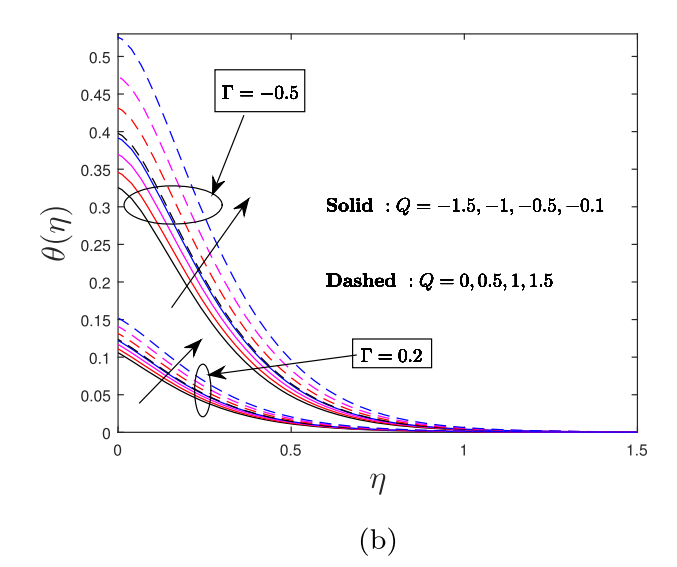
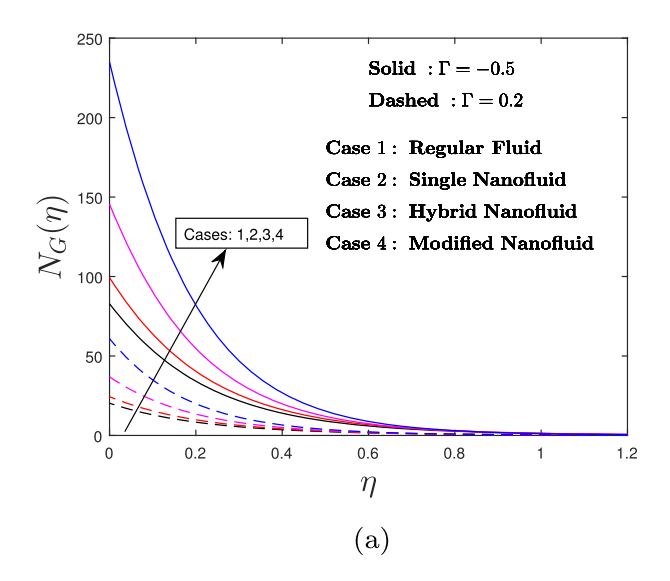


Figure 12: Thermal fields against different (a) γ and (b) Q.

velocity and temperature fields. In both stretching and shrinking instances, the figure shows that MNF velocity improves with escalation in λ , whereas the temperature decreases. This happens because greater suction strength in the flow leads to severe motion of the fluid, thus velocity is elevated and temperature is diminished. In actual fact, the thickness of momentum boundary layer is diminished leading to increment in velocity gradient at the surface, which in turn improves MNF velocity. As the external heat velocity is elevated, heat is spread quickly on all sides leading to a reduction in fluid temperature. Physically, larger values of λ reduces the thermal boundary layer

and surface temperature such that temperature gradient at the surface is enhanced and heat transmission from the hot plate to cool ambient becomes slower.

Figure 12 depicts the impact of Biot number (Bi), heat source (Q > 0), and heat sink (Q < 0) on the temperature curves. For both stretching and shrinking Riga surfaces, Figure 12a shows that upsurge in Bi leads to rapid increment in the temperature profiles of the MNF near the surface of the sheet owing to augmentation in the convective heat added onto the flow system. In physical sense, the Biot number is given as the convection at the surface of the hot body to the heat conduction within the



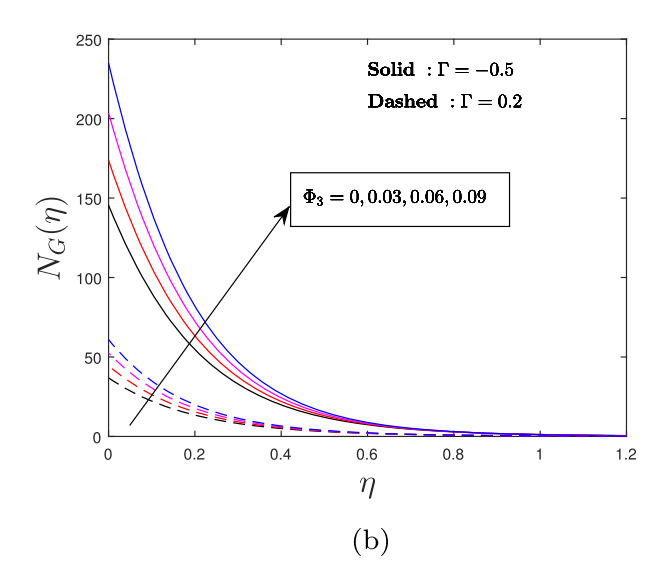
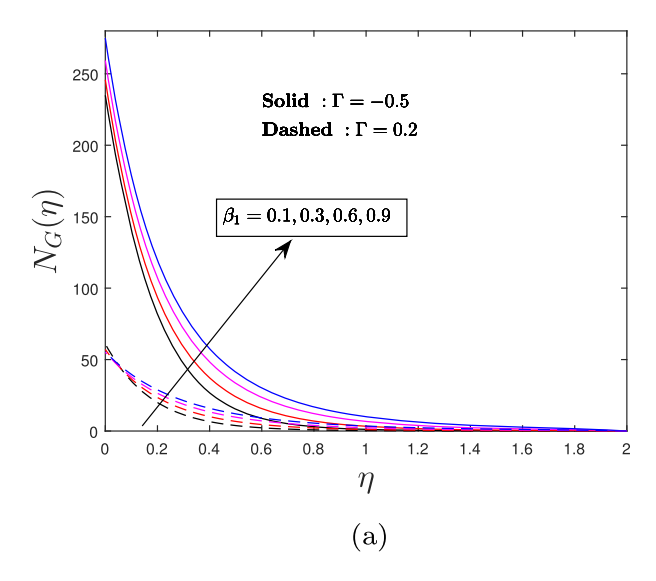
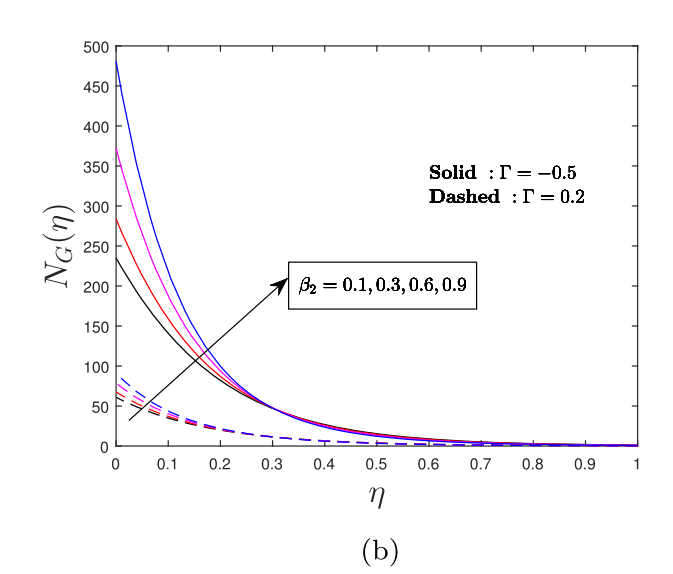


Figure 13: Behaviour of (a) regular fluid, SNF, HNF, MNF and (b) ϕ_3 on entropy generation.





surface of the hot body. Thus, for larger Bi, more heat is transmitted from the surface to the NPs giving rise to the MNF temperature. For low Bi, it can take a lot of time to transfer heat from the surface into the NPs; thus, MNF temperature cannot be raised rapidly enough. It is clear in Figure 12b that escalation in heat source parameter improves the temperature of the MNF when $\Gamma = -0.5$ and $\Gamma = 0.2$. Physically, the existence of heat source means heat is generated within the system in the course of the flow and extra heat is produced to the nanofluid, thus thickening the thermal boundary layer and improving temperature. In contrary, enhancement in the heat sink (-0.1 to -1.5) leads to a reduction in MNF temperature



and inter-related thermal boundary layer thickness. This is because negative values of Q correspond to heat absorption taking place in the system in course of the flow.

Figure 13 demonstrates the variation of different types of fluid models and volume fraction of Ni NPs against entropy generation. In both cases of stretching and shrinking Riga plate, the figure shows that more entropy is generated in the MNF when compared to the other fluids (conventional third-grade fluid, SNF, and HNF), where the conventional fluid illustrates least entropy generation. The high entropy associated with MNF is due to the augmentation of heat transmission with the use of more NPs of different kinds. As expected, increasing values of

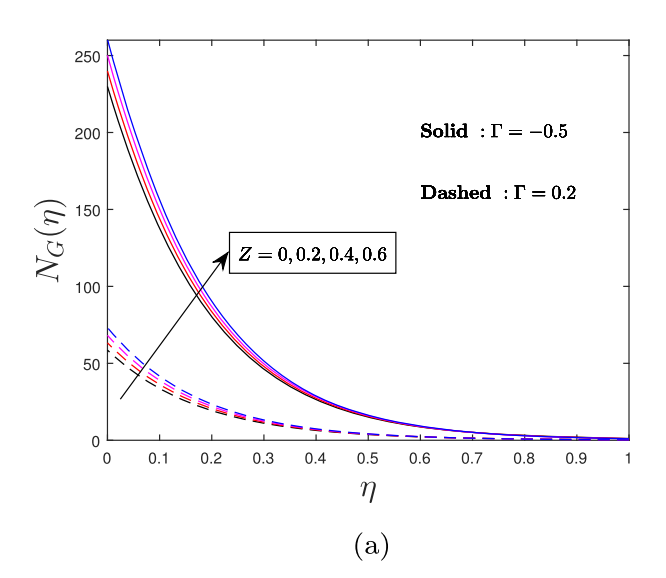
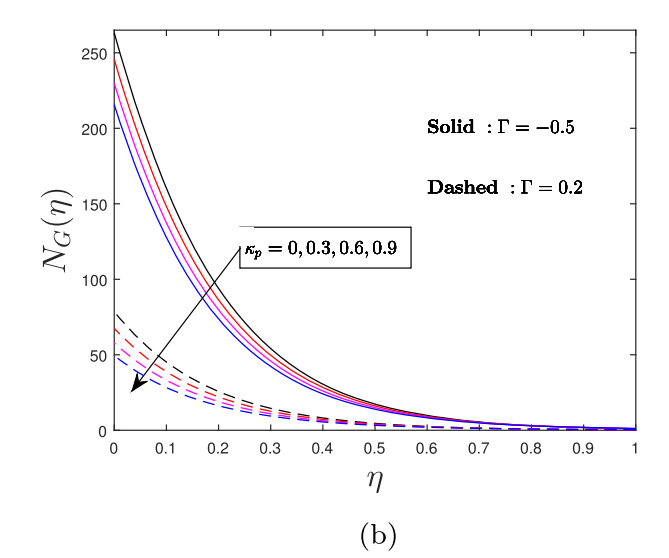
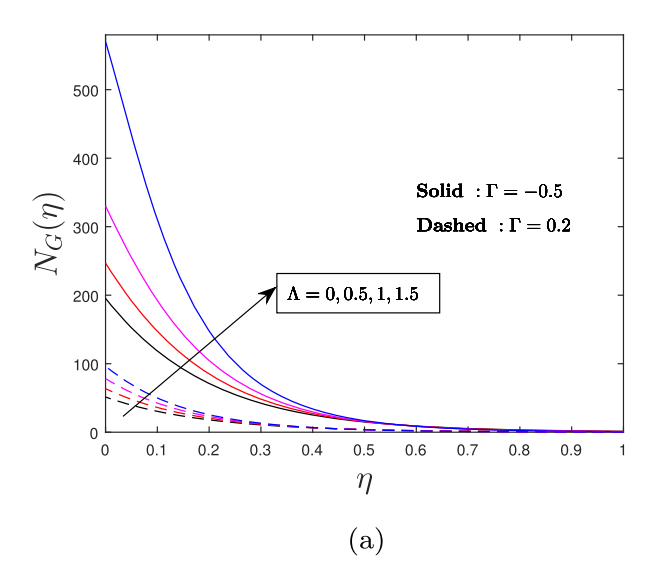


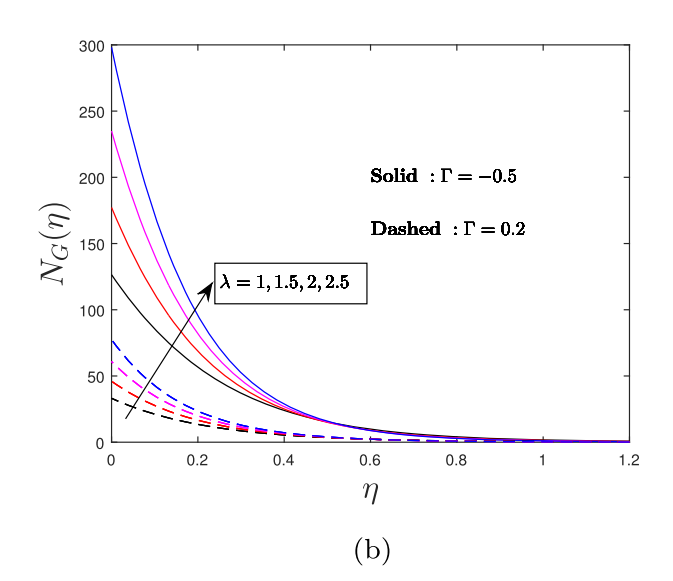
Figure 15: Entropy generation profiles against (a) Z and (b) k_p .





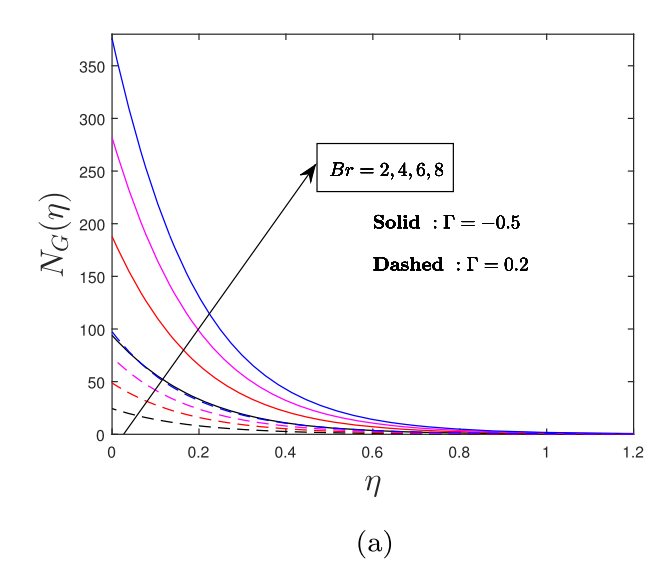


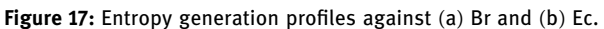
 Φ_3 also result to more entropy generation. The extra temperature in the flow due to large Φ_3 becomes exhausted from the system and causes an increment in the entropy production. Figure 14 elucidates that entropy minimization can be attained by depreciating the non-Newtonian third-grade parameters β_1 and β_2 in both stretching and shrinking cases. Figure 15a depicts that entropy generated is high with augmented modified Hartman number when $\Gamma=-0.5$ and $\Gamma=0.2$. This is to be expected since enhancement in Lorentz force due to augmented Z results in more friction that imposes upsurge in the rate of entropy generation. In contrary, entropy generation is lowered by high porosity parameter as shown in Figure 15b. This implies that the main intention of second law of thermodynamics, which is



entropy minimization can be ascertained by the inclusion of porous media in the flow system.

Figure 16 discloses that entropy production is increased by raising the variable viscosity (Λ) and suction ($\lambda > 0$) parameters in both cases of stretching and shrinking Riga plate. The enhancement of Λ leads to augmented fluid viscosity that generate resistance between fluid particles, thus disorder within the system augments resulting in enhanced entropy production. On a similar note, high suction strength relate to more entropy generated. This is because N_G is proportional to temperature and velocity gradients, whereas temperature and velocity gradients are directly correlated to suction, consequently entropy production enhances. Figure 17(a) elucidates that entropy generation profiles are raised





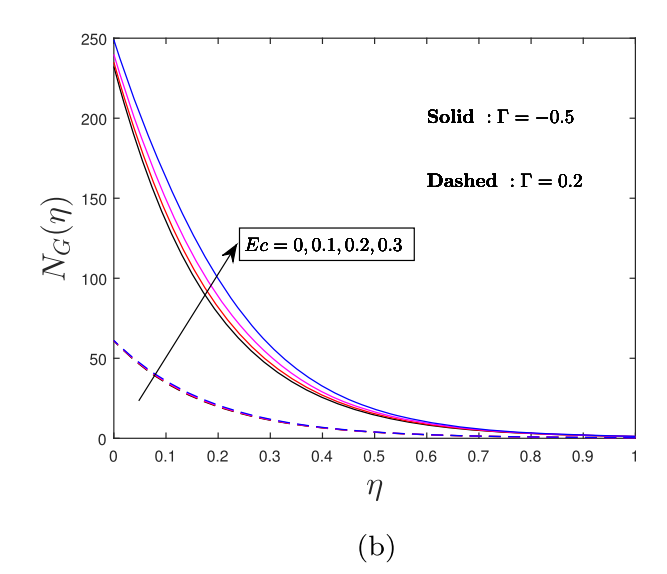


Table 8: Re $_{x}^{
u 2} \mathcal{C}_{eta}$ values for viscous fluid, single NF, hybrid NF and modified NF

R ₁ R ₂ R ₂ R ₃ Niscous fluid Single NF Hybrid NF Modified NF Viscous fluid Single NF Hybrid NF Modified NF Viscous fluid Single NF Hybrid NF No.24530 10.24783 2.484357 2.806369 3.623 3.223 3.235							Γ = -0.5			$\Gamma = 0.2$			
0.1 5.011517 5.671691 7.286126 10.062652 2.484357 2.806369 3.021503 5.269663 5.29803 7.545190 10.324783 2.700961 3.021503 3.021503 5.266606 6.187891 7.804246 10.587125 2.917348 3.235401 4.336601 6.20847 6.882281 7.415663 10.193694 2.592688 2.913968 3.315543 0.1 6.208847 6.882281 8.499590 11.309805 3.359290 3.692871 4.99590 0.1 6.140608 5.800754 7.415643 10.193694 2.59688 2.913968 3.416083 0.3 6.134933 6.812573 8.538986 11.433101 2.831066 3.416083 3.416083 0.5 7.561833 7.950962 9.785981 10.918798 3.416083 3.416083 4.41085 3.416083 4.41085 3.416083 3.416083 4.41085 3.416083 3.416083 4.41086 3.416083 3.416083 3.416083 3.416083 3.416083 3.416083 3.416083 3.416094 2.592688 2.913968 3.416083 <th>$oldsymbol{eta}_1$</th> <th>β_2</th> <th>k_p</th> <th><</th> <th>~</th> <th>Viscous fluid</th> <th>Single NF</th> <th>Hybrid NF</th> <th>Modified NF</th> <th>Viscous fluid</th> <th>Single NF</th> <th>Hybrid NF</th> <th>Modified NF</th>	$oldsymbol{eta}_1$	β_2	k_p	<	~	Viscous fluid	Single NF	Hybrid NF	Modified NF	Viscous fluid	Single NF	Hybrid NF	Modified NF
0.1 5.269663 5.929803 7.545190 10.324783 2.700961 3.021503 3.021503 1.0 5.27699 6.187891 7.804246 10.587125 2.917348 3.236401 3.236401 1.0 5.140608 5.800754 7.415663 10.193694 2.592688 2.913968 3.315543 2.913968 3.315543 2.913968 3.315543 2.913968 3.315543 2.913968 3.315543 2.913968 3.315543 2.913968 3.315543 2.913968 3.315543 2.913968 3.315543 2.913968 3.315543 2.913968 3.315543 2.913968 3.315543 2.913968 3.315543 2.913968 3.315543 3.3150843 3.315543 3.315543 <						5.011517	5.671691	7.286126	10.062652	2.484357	2.806369	3.622766	4.980459
0.1 5.527699 6.187891 7.804246 10.587125 2.917348 3.236401 4.836401 1.40608 5.800754 7.415663 10.193694 2.592688 2.913968 3.15543 5.666606 6.335111 7.952344 10.75156 2.986194 3.315543 2.913968 0.1 6.208847 6.882281 8.499590 11.309805 3.359290 3.692871 2.913968 0.3 6.134933 6.812573 8.538986 11.433101 2.831066 2.913968 0.3 7.261833 7.56962 9.785981 12.786838 3.416083 3.416083 0.5 7.261833 7.59062 9.785981 10.918798 3.030274 3.410056 0.3 5.23073 6.241739 7.949933 10.918798 3.030274 3.410056 0.3 5.23073 6.241739 7.619433 10.018798 3.20208 3.104962 0.4 4.356984 4.928577 6.319541 8.608102 2.297261 2.57578 0.4 4.750794 5.240608 5.34297 7.41563 1.91368 2						5.269663	5.929803	7.545190	10.324783	2.700961	3.021503	3.835675	5.190421
0.1 5.40608 5.800754 7.415663 10.193694 2.592688 2.913688 0.1 5.666606 6.335111 7.952344 10.75156 2.986194 3.31543 6.93871 0.1 6.208847 6.882281 8.499590 11.309805 3.359290 3.692871 6.292888 0.3 5.140608 5.800754 7.415663 10.193694 2.592688 2.913968 0.3 6.134933 6.812573 8.53896 11.433101 2.831066 3.156381 0.5 7.261833 7.550962 9.785981 12.786838 3.087688 3.41005 0.5 7.261833 7.950962 9.785981 10.918798 3.087688 3.41025 0.3 5.286043 5.968188 7.619433 10.470551 2.760988 3.104962 0.6 5.071469 5.721269 7.318487 10.061491 2.51738 2.822183 0.6 4.396984 4.928577 6.319541 8.608102 2.97261 2.74162 0.2 4.40608 5.800754 7.415663 10.193694 2.526488 2.913968<						5.527699	6.187891	7.804246	10.587125	2.917348	3.236401	4.048272	5.400097
0.1 5.666606 6.335111 7.952344 10.75156 2.986194 3.315543 2.08847 0.1 6.208847 6.882281 8.499590 11.309805 3.559290 3.692871 2.91368 0.1 5.140608 5.800754 7.415663 10.193694 2.592688 2.913968 0.3 6.134933 6.812573 8.538986 11.433101 2.831066 3.156381 4.16083 0.5 7.261833 7.950962 9.785981 12.786838 3.030274 3.416083 4.410053 0.5 6.233073 6.241739 7.949933 10.470551 2.760988 3.104962 0.6 5.253073 6.241739 7.619433 10.470551 2.760988 3.104062 0.6 5.071469 5.721269 7.318487 10.061491 2.51738 2.822183 0.6 4.396984 4.751269 7.415663 10.193694 2.592688 2.91368 0.4 5.140608 5.800754 7.415663 10.193694 2.552688 2.913968 1.5 4.470794 5.800754 7.415663 10.1	0.1					5.140608	5.800754	7.415663	10.193694	2.592688	2.913968	3.729262	5.085478
0.1 6.208847 6.882281 8.499590 11.309805 3.359290 3.692871 6.208871 2.93688 3.692871 6.1340608 5.800754 7.415663 10.193694 2.592688 2.913968 3.155381 6.315381 6.134933 6.812573 8.538986 11.433101 2.831066 3.155381 6.291368 3.416083 3.104962 3.41025 3.41025 3.41025 3.41025 3.41025 3.41025 3.41025 3.41025 3.41025 3.41025 3.41025 3.41025 3.41025 3.41025 3.41025 3.41025 3.41026 3.318487 4.42009 3.74102 3.51046 3.51046 3.510466 3.51046 3.51046 3.51046 3.51046 3.51046 3.51046 3.51046 3.51056 3.51056 3.51056 3.51056<	0.3					5.666606	6.335111	7.952344	10.75156	2.986194	3.315543	4.152197	5.543801
6.140608 5.800754 7.415663 10.193694 2.592688 2.913968 6.134933 6.812573 8.538986 11.433101 2.831066 3.156381 2.156381 0 7.261833 7.950962 9.785981 12.786838 3.087688 3.416083 0.3 5.223073 6.241739 7.949933 10.918798 3.030274 3.411025 0.3 5.286043 5.968188 7.619433 10.470551 2.760988 3.104962 0.6 4.396984 4.928577 6.319541 8.608102 2.297261 2.575758 0.2 4.751794 5.341951 6.83304 9.334297 2.442009 2.741162 0.4 5.140608 5.800754 7.41563 10.193694 2.592688 2.913968 1.5 4.470794 5.040117 6.386476 8.732093 2.250447 2.552180 2 5.140608 5.800754 7.415663 10.193694 2.592688 2.913968	0.5					6.208847	6.882281	8.499590	11.309805	3.359290	3.692871	4.540673	5.952713
0.3 6.134933 6.812573 8.538986 11.433101 2.831066 3.156381 2.831066 0 7.261833 7.950962 9.785981 12.786838 3.087688 3.416083 2.416083 0.3 5.523073 6.241739 7.949933 10.918798 3.030274 3.411025 2.411025 0.3 5.286043 5.968188 7.619433 10.470551 2.760988 3.104962 3.822183 0.6 4.396984 4.928577 6.319541 8.608102 2.297261 2.575758 3.827183 0.4 5.140608 5.800754 7.41563 10.193694 2.592688 2.913968 1.5 4.470794 5.040117 6.386476 8.732093 2.250447 2.555180 2 5.140608 5.800754 7.415663 10.193694 2.592688 2.913968		0.1				5.140608	5.800754	7.415663	10.193694	2.592688	2.913968	3.729262	5.085478
0 5.523073 7.950962 9.785981 12.786838 3.087688 3.416083 4.416083 3.416083 4.410025 4.410025 4.410025 4.410025 4.410025 4.410025 4.410025 4.410025 4.410025 4.410025 4.410025 4.410025 4.410025 4.410025 4.410025 4.41002 4.410		0.3				6.134933	6.812573	8.538986	11.433101	2.831066	3.156381	4.003183	5.391010
5.523073 6.241739 7.949933 10.918798 3.030274 3.411025 4.41025 5.286043 5.968188 7.619433 10.470551 2.760988 3.104962 5.071469 5.721269 7.318487 10.061491 2.511738 2.822183 0 4.396984 4.928577 6.319541 8.608102 2.297261 2.575758 0.2 4.751794 5.341951 6.83304 9.334297 2.442009 2.741162 0.4 5.140608 5.800754 7.415663 10.193694 2.592688 2.913968 1.5 4.470794 5.040117 6.386476 8.732093 2.250447 2.525180 2 5.140608 5.800754 7.415663 10.193694 2.592688 2.913968		0.5				7.261833	7.950962	9.785981	12.786838	3.087688	3.416083	4.294358	5.712751
5.286043 5.968188 7.619433 10.470551 2.760988 3.104962 6 5.071469 5.721269 7.318487 10.061491 2.511738 2.822183 0 4.396984 4.928577 6.319541 8.608102 2.297261 2.575758 0.2 4.751794 5.341951 6.83304 9.334297 2.442009 2.741162 0.4 5.140608 5.800754 7.415663 10.193694 2.592688 2.913968 1.5 4.470794 5.040117 6.386476 8.732093 2.250447 2.525180 2 5.140608 5.800754 7.415663 10.193694 2.592688 2.913968			0			5.523073	6.241739	7.949933	10.918798	3.030274	3.411025	4.302351	5.818064
0 4.396984 5.721269 7.318487 10.061491 2.511738 2.822183 0 4.396984 4.928577 6.319541 8.608102 2.297261 2.575758 0.2 4.751794 5.341951 6.83304 9.334297 2.442009 2.741162 0.4 5.140608 5.800754 7.415643 10.193694 2.592688 2.913968 1.5 4.470794 5.040117 6.386476 8.732093 2.250447 2.525180 2 5.140608 5.800754 7.415663 10.193694 2.592688 2.913968			0.3			5.286043	5.968188	7.619433	10.470551	2.760988	3.104962	3.950182	5.368262
4.396984 4.928577 6.319541 8.608102 2.297261 2.575758 4.751794 5.341951 6.83304 9.334297 2.442009 2.741162 5.140608 5.800754 7.415663 10.193694 2.592688 2.913968 1 3.862359 4.358171 5.465961 7.453135 1.927575 2.159616 1.5 4.470794 5.040117 6.386476 8.732093 2.250447 2.525180 2 5.140608 5.800754 7.415663 10.193694 2.592688 2.913968			9.0			5.071469	5.721269	7.318487	10.061491	2.511738	2.822183	3.622761	4.948965
4.751794 5.341951 6.83304 9.334297 2.442009 2.741162 5.140608 5.800754 7.415663 10.193694 2.592688 2.913968 1 3.862359 4.358171 5.465961 7.453135 1.927575 2.159616 1.5 4.470794 5.040117 6.386476 8.732093 2.250447 2.525180 2 5.140608 5.800754 7.415663 10.193694 2.592688 2.913968				0		4.396984	4.928577	6.319541	8.608102	2.297261	2.575758	3.32554	4.547932
5.140608 5.800754 7.415663 10.193694 2.592688 2.913968 3.913968 1 3.862359 4.358171 5.465961 7.453135 1.927575 2.159616 3.252180 1.5 4.470794 5.040117 6.386476 8.732093 2.250447 2.525180 2 5.140608 5.800754 7.415663 10.193694 2.592688 2.913968				0.2		4.751794	5.341951	6.83304	9.334297	2.442009	2.741162	3.522598	4.809045
4.358171 5.465961 7.453135 1.927575 2.159616 2.504017 5.040117 6.386476 8.732093 2.250447 2.525180 5.800754 7.415663 10.193694 2.592688 2.913968				0.4		5.140608	5.800754	7.415663	10.193694	2.592688	2.913968	3.729262	5.085478
4 5.040117 6.386476 8.732093 2.250447 2.525180 3 5 5.800754 7.415663 10.193694 2.592688 2.913968					1	3.862359	4.358171	5.465961	7.453135	1.927575	2.159616	2.707937	3.634331
3 5.800754 7.415663 10.193694 2.592688 2.913968 3					1.5	4.470794	5.040117	6.386476	8.732093	2.250447	2.525180	3.202835	4.336298
					2	5.140608	5.800754	7.415663	10.193694	2.592688	2.913968	3.729262	5.085478

Table 9: Re_x¹²²Nu_x values for viscous fluid, single NF, hybrid NF and modified NF

							. = _	r = -0.5			<u>"</u>	r = 0.2	
7	$oldsymbol{eta}_1$	k_p	<	, ,	7 O								Viscous fluid
						Single NF			Hybrid NF	Modified NF			Viscous fluid
						Single NF			Hybrid NF	Modified NF			
0.2						0.384847	0.370771	0.340168	0.287641	0.458688	0.455286	0.447844	0.435597
9.0						0.37885	0.364651	0.333754	0.280979	0.456229	0.452785	0.445209	0.432881
9.0						0.372638	0.358334	0.327187	0.274201	0.453585	0.450117	0.442444	0.430069
	0.1					0.381876	0.367736	0.336981	0.284324	0.457482	0.454057	0.446543	0.434251
	0.2					0.37158	0.357153	0.326299	0.273269	0.455188	0.451708	0.444202	0.431848
	0.3					0.361252	0.346583	0.315691	0.262439	0.452885	0.449364	0.441884	0.429519
		0.1				0.372393	0.356633	0.32331	0.265764	0.452666	0.448462	0.439792	0.425353
		0.3				0.377332	0.362421	0.330411	0.275391	0.45521	0.451421	0.443343	0.430018
		0.5				0.381876	0.367736	0.336981	0.284324	0.457482	0.454057	0.446543	0.434251
			0			0.392977	0.381022	0.354094	0.309818	0.459668	0.456606	0.449685	0.438544
			0.2			0.387632	0.374662	0.345976	0.297967	0.458597	0.455359	0.448149	0.436452
			0.4			0.381876	0.367736	0.336981	0.284324	0.457482	0.454057	0.446543	0.434251
				0.1		0.078932	0.076063	0.069742	0.058894	0.094455	0.093793	0.092264	0.089741
				0.3		0.232897	0.224352	0.205647	0.173584	0.278857	0.276834	0.272287	0.264816
				0.5		0.381876	0.367736	0.336981	0.284324	0.457482	0.454057	0.446543	0.434251
				τ,	_	0.296092	0.271138	0.225708	0.143909	0.428622	0.423588	0.413998	0.398269
				τ,	1.5	0.356015	0.338912	0.303951	0.243138	0.447828	0.443877	0.435677	0.422231
				, 4	2	0.381876	0.367736	0.336981	0.284324	0.457482	0.454057	0.446543	0.434251
					-0.5		0.385341	0.358878	0.315194	0.461282	0.458498	0.451946	0.441564
					-0-		0.380656	0.353059	0.307086	0.460247	0.457294	0.450483	0.4396
					0.2		0.373656	0.344355	0.294832	0.458733	0.455526	0.448332	0.436691
					0.5		0.367736	0.336981	0.284324	0.457482	0.454057	0.446543	0.434251

with high Brinkman number (Br) in both cases of shrinking and stretching surface. The Brinkman number is sensitive to improve the friction of nanofluid which results in more entropy generated. Accordingly, Br manages the omitting of heat via viscous heating in correlation to heat transmission in the company of molecular conduction. Heat omitted by viscous impact is lower than heat transmission by molecular conduction near the surface. As a result, superior amount of heat is formed between layers of the fluid particles in motion, leading to enhancement in entropy production. An increase in the chaotic behaviour of the overall system is evident to be generating more heat in the system because of higher values of Br. From Figure 17(b), N_G is directly correlated with the Eckert number and that is why increment in Ec implies more entropy generated. This is justified by the fact that frictional heating rises with escalating Ec.

The impact of various important flow parameters on the physical quantities of interest for varying types of fluids when $\Gamma = -0.5$ (shrinking sheet) and $\Gamma = 0.2$ (stretching sheet) is demonstrated in Tables 8 and 9. From Table 8, higher wall shear stress corresponds to the shrinking surface and MNF model, whereas lower wall shear stress belongs to the stretching surface and conventional thirdgrade fluid. It is noticeable that the values of skin friction coefficients in the MNF model are almost double those values in the conventional third-grade fluid. From Table 9, higher Nusselt numbers correspond to the stretching surface and conventional third-grade fluid, whereas lower Nusselt numbers belongs to the shrinking surface and MNF model. These results are similar to those found by Khashi'e et al. [18] in the second-grade HNF model. The higher wall shear stress and low rate of heat transfer associated with MNF are due to the fact that inserting more or diverse NPs result in superior energy transportation *via* the flow in relation with the irregular movement of NPs. The skin friction coefficient also enhances with higher variable fluid viscosity, suction strength, EMHD, and non-Newtonian thirdgrade parameters, but depreciates with the existence of porous media. On the other hand, the heat transmission rate improves with growing suction strength, porous media, and heat sink, but diminishes with increment in variable fluid viscosity, Biot number, heat source, EMHD, and non-Newtonian third-grade parameters.

5 Concluding remarks

This study highlights analysis of entropy generated, stagnation point flow, and heat transfer on a third-grade

modified HNF model driven by a stretchable/shrinkable Riga plate in a porous medium with heat-dependent fluid viscosity. The modified hybrid nanofluid has been prepared by suspending solid NPs of Cu, Al₂O₃ and Ni into the host fluid (pure water) in a particular order. The mathematical model also incorporates the impacts of heat omission/consumption, convective boundary conditions, suction/injection, and viscous dissipation in the boundary layer region. The performance of each type of fluid and various controlling parameters on entropy generated, velocity, temperature, and physical quantities of interest has also been investigated. Although utilization of appropriate transformations the governing mathematical equations are transmuted into nonlinear ODEs that are numerically solved via SQLM that is executed on overlapping multi-domains. The choice of overlapping grid approach over the single-domain approach is justified through the analysis of residual and solution errors, condition numbers, execution time, and error bound theorems. The error bound theorem discloses that the error in univariate polynomial interpolation is substantially smaller when interpolation is carried out on partitioned domain than on a single fixed domain. Also, the residual error estimates and condition numbers are notable to be very small in the overlapping domain decomposition approach leading to computation of highly accurate and stable results in a short runtime using few grid points and iterations. As a comparative scrutiny, it is perceived that MNF plays an efficient role in the intensification of thermal conductance when collated with HNF, SNF, and conventional third-grade fluid. The rest of the valuable findings include that:

- Fluid flow accelerates with more NPs of different type (MNF model), high EMHD, and variable fluid parameter, whereas decelerates with increasing third-grade and porosity parameters.
- Temperature and thickness of the thermal boundary layer enhance with variable fluid viscosity, Biot number, and heat source, but decrease with suction strength and heat sink.
- Entropy of the system is enhanced by increasing the Brinkman number, third-grade parameters, EMHD, variable fluid viscosity, suction strength, and viscous dissipation, and by using the MNF model, but minimized by including the porous media in the flow system.
- Wall drag coefficient improves with large Λ , λ , Z and β_1 , and low k_p , whereas heat transmission rate enhances with high λ and k_p , and least Λ , Bi, Z, and β_1 .
- MNF and shrinking surface yield maximum skin friction when compared to conventional third-grade fluid,

Subscripts ∞ , w

 s_1, s_2, s_3

nf, hnf, mnf

SNF and HNF. The opposite is true with regard to the rate of heat transmission.

Due to superior thermal conductivity, stability, chemically inertness, cost-effectiveness, and environmental friendly of the considered non-Newtonian third-grade modified hybrid nanofluid model accompanied by the controlling parameters, it can be of practical use in various engineering and industrial applications where thermal improvement is important. The outcomes of this scrutiny can be used to drive future progress in which thermal proficiency of thermal system can be ascertained via dispersion of various types of NPs into other non-Newtonian fluids such as Maxwell, fourth-grade, Carreau, Williamson, tangent hyperbolic, Carreau-Yasuda, Jeffery, and micropolar fluids. Future works on modified hybrid nanofluid can also use the obtained results to validate newly computed results. The merits demonstrated by the employed numerical method indicate that it can be utilized as a bench-marking tool for previous and future studies on similar flow problems.

Nomenclature

Roman letters	
u, v	velocity segments (m s^{-1})
<i>x</i> , <i>y</i>	cylindrical coordinates (m)
u_w	Riga plate velocity (m s^{-1})
u_e	free stream velocity (m s^{-1})
$\nu_{\scriptscriptstyle W}$	mass transfer velo-
	city $(m \ s^{-1})$
h_f	convective heat transfer
	coefficient (W $m^{-2}K^{-1}$)
<i>k</i> *	permeability (m^2)
j_0	applied current density in
	the electrodes (A m^{-2})
M	magnetization of the per-
	manent magnets mounted
	on the Riga plate surface (T)
b_1	width of electrodes and
	magnets (m)
Q_0	heat source/sink coeffi-
	cient (W $\mathrm{m}^{-3}\mathrm{K}^{-1}$)
а	positive constant (s^{-1})
С	constant signifying plate
	velocity (s ⁻¹)
T	fluid temperature (K)
T_w , T_∞	wall and ambient tempera-
	ture (K)
Ср	specific heat at constant
	pressure (J $\mathrm{Kg^{-1}}\mathrm{K^{-1}})$

q_w	wall heat flux (W m^{-2})
$S_g^{\prime\prime\prime}$	local volumetric entropy
	generation rate (W $m^{-3} K^{-1}$)
S_0'''	characteristic entropy gen-
	eration rate (W $\mathrm{m}^{-3}\mathrm{K}^{-1}$)
N_G	entropy generation
	parameter
$f(\eta)$	velocity similarity function
Z	modified Hartmann number
k_p	porosity parameter
Re_x	local Reynolds number
Ec	Eckert number
Pr	Prandtl number
Q	heat source/sink parameter
Br	Brinkman number
C_f , Nu_x	skin friction coefficient via
	the <i>x</i> -direction and local
	Nusselt number
Greek symbols	

,	
η	similarity variable
μ	fluid dynamic visc-
	osity (Kg m^{-1} s ⁻¹)
κ	fluid thermal conduc-
	tivity (W $m^{-1} K^{-1}$)
ρ	fluid density (Kg m ⁻³)
$ au_{xy}$	wall shear
•	stress (Kg $\mathrm{m}^{-1}\mathrm{s}^{-2})$
ξ_t	non-dimensional tempera-
	ture variance (m)
$\beta_1, \beta_2, \beta_3$	third-grade fluid parameters
Φ_1 , Φ_2 , Φ_3	solid volume fraction of
	aluminium oxide, copper,
	and nickel NPs
Ω_1	width of the electrodes and
	magnets
Λ	temperature-variant visc-
	osity parameter
y	Biot number
Γ	velocity ratio parameter
λ	mass transpiration
	parameter
θ	non-dimensionless
	temperature

Ambient and wall conditions

conventional fluid

nanofluids

solid NPs of aluminium oxide, copper and nickel

single, hybrid and modified

Acknowledgments: The authors would like to express their gratitude to the college of Science, Engineering and Technology (CSET) and Department of Mathematical Sciences, University of South Africa for providing the financial support. The authors also appreciate the respected editorials, and anonymous reviewers for their constructive suggestions.

Funding information: There is no funding to declare for this research study.

Author contributions: All authors have accepted responsibility for the entire content of this manuscript and approved its submission.

Conflict of interest: The authors declare that they have no competing interests.

References

- [1] Fosdick RL, Rajagopal KR. Thermodynamics and stability of third grade. Proc R Soc A. 1980;339:351-77.
- [2] Lee KJ, Yoon SH, Jang J. Carbon nanofibers: a novel nanofiller for nanofluid applications. Small. 2007;3:1209-13.
- [3] Choi SU, Eastman JA. Enhancing thermal conductivity of fluids with nanoparticles. ASME-Publications-Fed. 1995;231:99-105.
- [4] Das PK, Mallik AK, Ganguly R, Santra AK. Synthesis and characterization of TiO2-water nanofluids with different surfactants. Int Commun Heat Mass Transf. 2016;75:341–8.
- [5] Mintsa HA, Roy G, Nguyen CT, Doucet D. New temperature dependent thermal conductivity data for water-based nanofluids. Int J Therm Sci. 2009;48:363-71.
- [6] Zhu H, Zhang C, Liu S, Tang Y, Ying Y. Effects of nanoparticle clustering and alignment on thermal conductivities of Fe3O4 aqueous nanofluids. Appl Phys Lett. 2006;89(2):023123.
- [7] Raja MAZ, Tabassum R, El-Zahar ER, Shoaib M, Khan MI, Malik MY, et al. Intelligent computing through neural networks for entropy generation in MHD third-grade nanofluid under chemical reaction and viscous dissipation. Waves Random Complex Media. 2022. In Press. doi: 10.1080/17455030.2022.2044095.
- [8] Zeeshan, Shaikh GM. Analysis of temperature-dependent viscosity effect on wire coating using MHD flow of incompressible third-grade nanofluid filled in cylindrical coating die. Adv Mech Eng. 2022;14(4):1–14.
- [9] Ali K, Faridi AA, Ahmad S, Jamshed W, Khan N, Alam MM. Quasi-linearization analysis for heat and mass transfer of magnetically driven 3rd-grade (Cu-TiO2/engine oil) nanofluid via a convectively heated surface. Int Commun Heat Mass Transf. 2022;135:106060.
- [10] Khan SA, Hayat T, Alsaedi A. Melting heat in entropy optimized flow of third grade nanomaterials with radiation by a Riga plate. J Energy Storage. 2022;45:103713.
- [11] Krishna MV, Ahammad NA, Algehyne EA. Unsteady MHD thirdgrade fluid past an absorbent high-temperature shrinking

- sheet packed with silver nanoparticles and non-linear radiation. J Taibah Univ Sci. 2022;16(1):585-93.
- [12] Buongiorno J. Convective transport in nanofluids. ASME J Heat Transf. 2006;128(3):240-50.
- [13] Tiwari RK, Das MK. Heat transfer augmentation in two-sided lid-driven differentially heated square cavity utilizing nanofluids. Int J Heat Mass Transf. 2007;50:2002–18.
- [14] Suresh S, Venkitaraj KP, Selvakumar P, Chandrasekar M. Synthesis of Al₂O₃-Cu/water hybrid nanofluids using two step method and thermophysical properties. Colloids Surf A Physicochem Eng Asp. 2011;388(1–3):41–8.
- [15] Suresh S, Venkitaraj KP, Selvakumar P, Chandrasekar M. Effect of Al_2O_3 -Cu/water hybrid nanofluid in heat transfer. Exp Therm Fluid Sci. 2012;38:54–60.
- [16] Devi SPA, Devi SSU. Numerical investigation of hydromagnetic hybrid Cu-Al2O3/water nanofluid flow over a permeable stretching sheet with suction. Int J Nonlinear Sci Numer Simul. 2016;17(5):249–57.
- [17] Khashi'ie NS, Waini I, Kasim ARM, Zainal NA, Arifin NM, Pop I. Thermal progress of a non-Newtonian hybrid nanofluid flow on a permeable Riga plate with temporal stability analysis. Chin J Phys. 2022;77:279–90.
- [18] Khashi'ie NS, Waini I, Zokri SM, Kasim ARM, Arifin NM, Pop I. Stagnation point flow of a second-grade hybrid nanofluid induced by a Riga plate. Int J Numer Methods Heat Fluid Flow. 2022;32(7):2221–39.
- [19] Siddique I, Khan Y, Nadeem M, Awrejcewicz J, Bilal M. Significance of heat transfer for second-grade fuzzy hybrid nanofluid flow over a stretching/shrinking Riga wedge. AIMS Math. 2022;8(1):295–316.
- [20] Govindarajulu K, Reddy AS. Magnetohydrodynamic pulsatile flow of third grade hybrid nanofluid in a porous channel with Ohmic heating and thermal radiation effects. Phys Fluids. 2022:34:013105.
- [21] Adun H, Kavaz D, Dagbasi M. Review of ternary hybrid nanofluid: Synthesis, stability, thermophysical properties, heat transfer applications, and environmental effects. J Cleaner Prod. 2021;328:129525.
- [22] Arif M, Kumam P, Kumam W, Mostafa Z. Heat transfer analysis of radiator using different shaped nanoparticles water-based ternary hybrid nanofluid with applications: a fractional model. Case Stud Therm Eng. 2022;31:101837.
- [23] Hou E, Wang F, Nazi U, Sohail M, Jabbar N, Thounthong P. Dynamics of tri-hybrid nanoparticles in the rheology of pseudo-plastic liquid with Dufour and Soret effects. Micromachines. 2022;13:201.
- [24] Sohail M, El-Zahar ER, Mousa AAA, Nazir U, Althobaiti S, Althobaiti A, et al. Finite element analysis for ternary hybrid nanoparticles on thermal enhancement in pseudo-plastic liquid through porous stretching sheet. Sci Rep. 2022;12:9219.
- [25] Gul T, Saeed A. Nonlinear mixed convection couple stress trihybrid nanofluids flow in a Darcy-Forchheimer porous medium over a nonlinear stretching surface. Waves Random Complex Media. 2022. In Press. doi: 10.1080/17455030.2022.2077471.
- [26] Mehta KN, Sood S. Transient free convection flow with temperature dependent viscosity in a fluid saturated porous medium. Int J Eng Sci. 1992;30:1083-7.
- [27] Saeed A, Kumam P, Gul T, Alghamdi W, Kumam W, Khan A. Darcy-Forchheimer couple stress hybrid nanofluids flow with variable fluid properties. Sci Rep. 2021;11:19612.

[28] Alhussain ZA, Tassaddig A. Thin film blood Casson hybrid nanofluid flow with variable viscosity. Arab J Sci Eng. 2022;47:1087-94.

DE GRUYTER

- [29] Nadeem S, Abbas N. Effects of MHD on modified nanofluid model with variable viscosity in a porous medium. In: Kandelousi MS, Ameen S, Akhtar MS, Shin H, editors. Nanofluid Flow in Porous Media. London, UK: IntechOpen; 2019. doi: 10.5772/intechopen.84266.
- [30] Abbas N, Nadeem S, Saleem S, Issakhov A. Transportation of modified nanofluid flow with time dependent viscosity over a Riga plate: Exponentially stretching. Ain Shams Eng J. 2021;12(4):3967-73.
- [31] Ramesh GK, Madhukesh JK, Shehzad SA, Rauf A. Ternary nanofluid with heat source/sink and porous medium effects in stretchable convergent/divergent channel. Proc Inst Mech Eng E J Process Mech Eng. In Press. 2022. doi: 10.1177/ 09544089221081344.
- [32] Alharbi KAM, Ahmed AES, Sidi MO, Ahammad NA, Mohamed A, El-Shorbagy MA, et al. Computational valuation of Darcy Ternary-hybrid nanofluid flow across an extending cylinder induction effects. Micromachines. 2022;13(4):588.
- [33] Pandey AK, Kumar M. Natural convection and thermal radiation influence on nanofluid flow over a stretching cylinder in a porous medium with viscous dissipation. Alex Eng J. 2017;56(1):55-62.
- [34] Joshi N, Pandel AK, Upreti H, Kumar M. Mixed convection flow of magnetic hybrid nanofluid over a bidirectional porous surface with internal heat generation and a higher-order chemical reaction. Heat Transf. 2021;50(4):3661-82.
- [35] Singh K, Pandey AK, Kumar M. Numerical solution of micropolar fluid flow via stretchable surface with chemical reaction and melting heat transfer using Keller-Box method. Propuls Power Res. 2021;10(2):194-207.
- [36] Singh K, Pandey Ak, Kumar M. Numerical approach for chemical reaction and suction/injection impacts on magnetic micropolar fluid flow through porous wedge with Hall and ionslip using Keller Box method. Waves Random Complex Media. 2021. In Press. doi: 10.1080/17455030.2021.1988757.
- [37] Joshi N, Upreti H, Pandey AK, Kumar M. Heat and mass transfer assessment of magnetic hybrid nanofluid flow via bidirectional porous surface with volumetric heat generation. Int J Appl Comput Math. 2021;7:64.
- [38] Joshi N, Upreti H, Pandey AK. MHD Darcy-Forchheimer Cu-Ag/ H2O-C2H6O2 hybrid nanofluid flow via a porous stretching sheet with suction/blowing and viscous dissipation. Int J Comput Methods Eng. 2022;23(6):527-35.
- [39] Malik R, Khan M, Munir A, Khan WA. Flow and heat transfer in Sisko fluid with convective boundary conditions. PLoS One. 2014:9:e107989.
- [40] Singh K, Pandey AK, Kumar M. Entropy generation impact on flow of micropolar fluid via an inclined channel with non-uniform heat source and variable fluid properties. Int J Appl Comput Math. 2020;6:85.
- [41] Upreti H, Pandey AK, Kumar M. Assessment of entropy generation and heat transfer in three-dimensional hybrid nanofluids flow due to convective surface and base fluids. J Porous media. 2021;24(3):35-50.
- [42] Aziz A. A similarity solution for laminar thermal boundary layer over a flat plate with convective surface boundary condition. Comm Nonlinear Sci Num Simul. 2009;14(4):1064-8.

- [43] Gailitis A, Lielausis O. On a possibility to reduce the hydrodynamic resistance of a plate in an electrolyte. Appl Magn Rep Phys Inst. 1961;12:143-6.
- [44] Wahid NS, Arifin NM, Khashi'ie NS, Pop I, Bachok N, Hafidzuddin MEH. Hybrid nanofluid stagnation point flow past a slip shrining Riga plate. Chin J Phys. 2022;78:180-93.
- [45] Nidhi, Kumar L. Cu-Al2O3/engine oil Williamson nanofluid over a stretching/shrinking Riga plate with viscous dissipation and radiation effect. Heat Transf. 2022;51(2):2279-305.
- [46] Zainal NA, Nazar R, Naganthran K, Pop I. Unsteady stagnation point flow past a permeable stretching/shrinking Riga plate in Al2O3-Cu/H2O HNF with thermal radiation. Int J Numer Methods Heat Fluid Flow. 2022;32(8):2640-58.
- [47] Upreti H, Pandey AK, Uddin Z, Kumar M. Thermophoresis and Brownian motion effects on 3D flow of Casson nanofluid consisting microorganisms over a Riga plate using PSO: a numerical study. Chin J Phys. 2022;78:234-70.
- [48] Upreti H, Pandey AK, Kumar M. Unsteady squeezing flow of magnetic hybrid nanofluids within parallel plates and entropy generation. Heat Transf. 2021;50(1):105-25.
- [49] Huminic G, Huminic A. Entropy generation of nanofluid and hybrid nanofluid flow in thermal systems: a review. J Mol Liq. 2020;302:112533.
- [50] Souby MM, Bargal MHS, Wang Y. Thermohydraulic performance improvement and entropy generation characteristics of a microchannel heat sink cooled with new hybrid nanofluids containing ternary/binary hybrid nanocomposites. Energy Sci Eng. 2021;9(12):2493-513.
- [51] Sahoo RR. Heat transfer and second law characteristics of radiator with dissimilar shape nanoparticle-based ternary hybrid nanofluid. J Therm Anal Calorim. 20221;146(2):827-39.
- Khashi'ie NS, Arifin NM, Sherement M, Pop I. Shape factor effect of radiative Cu-Al2O3/H2O hybrid nanofluid flow towards an EMHD plate. Case Stud Therm Eng. 2021:26:101199.
- [53] Oztop HF, Abu-Nada E. Numerical study of natural convection in partially heated rectangular enclosures filled with nanofluids. Int J Heat Fluid Flow. 2008;29:1326-36.
- [54] Hou E, Wang F, Nazir U, Sohail M, Jabbar N, Thounthong P. Dynamics of tri-Hybrid nanoparticles in the rheology of pseudo-plastic liquid with Dufour and Soret effects. Micromachines. 2022;13:201.
- [55] Khan MI, Khan SA, Hayat T, Alsaedi A. Entropy optimization in magnetohydrodynamic flow of third-grade nanofluid with viscous dissipation and chemical reaction. Iran J Sci Technol Trans Sci. 2019;43:2679-89.
- [56] Mkhatshwa MP, Motsa SS, Ayano MS, Sibanda P. MHD mixed convective nanofluid flow about a vertical slender cylinder using overlapping multi-domain spectral collocation approach. Case Stud Therm Eng. 2020;18:100598.
- Mkhatshwa MP, Motsa SS, Sibanda P. Overlapping multi-[57] domain spectral method for MHD mixed convection slip flow over an exponentially decreasing mainstream with non-uniform heat source/sink and convective boundary conditions. Int J Comput Methods. 2021;18(5):2150004.
- [58] Mkhatshwa MP, Motsa SS, Sibanda P. MHD mixed convection flow of couple stress fluid over an oscillatory stretching sheet with thermophoresis and thermal diffusion using the overlapping multi-domain spectral relaxation approach. Int J Appl Comput Math. 2021;7:93.

- [59] Mkhatshwa MP, Khumalo M. Irrecersibility scrutinization on EMHD Darcy-Forchheimer slip flow of Carreau hybrid nanofluid through a stretchable surface in porous medium with temperature-variant properties. Heat Transf. 2022;52(1):359–429.
- [60] Mburu ZM, Nayak MK, Mondal S, Sibanda P. Impact of irreversibility ratio and entropy generation on three-dimensional Oldroyd-B fluid flow with relaxation-retardation viscous dissipation. Indian J Phys. 2022;96:151-67.
- [61] Bellman RE, Kalaba RE. Quasilinearization and Nonlinear Boundary Value Problems. Santa Monica (CA), USA: RAND Corporation; 1965.
- [62] Trefethen LN. Spectral Methods in Matlab. Philadelphia (PA), USA: SIAM; 2000.
- [63] Canuto C, Hussaini MY, Quarteroni A, Zang TA. Spectral Methods in Fluid Dynamics. Berlin, Germany: Springer; 1988.
- [64] Wang CY. Stagnation flow towards a shrinking sheet. Int J Non Lin Mech. 2008;43:377–82.
- [65] Bachok N, Ishak A, Pop I. Stagnation-point flow over a stretching/shrinking sheet in a nanofluid. Nanoscale Res Lett. 2011;6:623.
- [66] Yacob NA, Ishak A, Pop I. Falkner-Skan problem for a static or moving wedge in nanofluids. Int J Thermal Sci. 2011;50:133-9.